



# The Lucy Long Range Reconnaissance Imager (L'LORRI)

H.A. Weaver<sup>1</sup> · J.P. Wilson<sup>1</sup> · S.J. Conard<sup>1</sup> · J.D. Adams<sup>1</sup> · S. Begley<sup>1</sup> · J. Burgum<sup>1</sup> · E.H. Darlington<sup>1</sup> · N. Dello Russo<sup>1</sup> · R. Hacala<sup>1</sup> · S. London<sup>1</sup> · M.F. Morgan<sup>1</sup> · G. Murphy<sup>1</sup> · T. Nelson<sup>1</sup> · A. Shah<sup>1</sup> · J.R. Spencer<sup>2</sup> · H. Taylor<sup>1</sup> · T. Boehmer<sup>1</sup> · L. Burke<sup>1</sup> · C. Drabenstadt<sup>1</sup> · C. Henry<sup>1</sup> · S. Ling<sup>1</sup> · C. Porter<sup>1</sup> · J. Yin<sup>1</sup>

Received: 27 July 2023 / Accepted: 20 November 2023 / Published online: 30 November 2023  
© The Author(s) 2023

## Abstract

NASA's *Lucy* mission spacecraft was launched on 16 October 2021 and will perform the initial in situ investigation of the Jovian Trojan asteroids (Levison et al. 2021, 2024). The Lucy LOng Range Reconnaissance Imager (L'LORRI) is a panchromatic visible light (420–795 nm, 50% QE points), narrow-angle (field of view =  $0.29^\circ$ ), high spatial resolution ( $1.0'' \text{ pixel}^{-1}$ ) imager used on the *Lucy* mission for both science observations and optical navigation. L'LORRI is designed to provide maps of the sunlit portions of the Trojan surfaces to a resolution of  $\sim 10$  m (after deconvolution), which will enable crater counting to constrain the surface ages. L'LORRI's high sensitivity and large dynamic range permits imaging of the low albedo Trojans at moderately large phase angles (down to  $I/F$  values of  $\sim 0.0014$  with  $\text{SNR} \approx 30$  using an exposure time of 100 ms), as well as providing early acquisitions of the Trojans during the approach phase, searches for Trojan activity that are  $\sim 10\times$  better than can be obtained from Earth, and deep searches for potential Trojan satellites down to  $V \approx 20.4$  at spatial resolutions far surpassing that available from Earth. This paper describes the L'LORRI instrument design and the requirements that drove the design. We present results from L'LORRI's ground calibration campaign, summarize the L'LORRI in-flight calibration plan, and describe typical L'LORRI operations scenarios during the Trojan flybys. We also present an analysis of in-flight data taken during the first year of *Lucy* operations, which show that most aspects of L'LORRI's performance are nominal (i.e., as predicted), but the telescope's point spread function is slightly degraded relative to pre-flight predictions. Nevertheless, L'LORRI is still expected to fulfill all of its scientific objectives, which should revolutionize our view of the Jovian Trojans.

**Keywords** Trojan asteroids · Asteroids · Kuiper belt objects · Instruments · Cameras

## 1 Introduction

The *Lucy* mission is a NASA Discovery program that was selected in 2016 to perform the first in situ exploration of the Jovian Trojan asteroids (Levison et al. 2021, 2024). These Trojans are thought to have been emplaced in the Lagrange L4 and L5 regions early in the solar system's history during the radial migration of the giant planets (cf. Nesvorný et al. 2013) and most have been in dynamically stable orbits for the past 4.5 Gyr. As such, the

---

Extended author information available on the last page of the article

Jovian Trojans are fossil remnants that may provide a unique tracer of the solar system's early dynamical, physical, and chemical evolution.

The Lucy LOng Range Reconnaissance Imager (L'LORRI) is a panchromatic visible light camera that will provide the highest resolution images of the surfaces of the bodies targeted for flybys during the *Lucy* mission. These images will be used to perform detailed geological mapping of the surfaces of the *Lucy* targets, which will enable crater counting to constrain the ages of these surfaces. L'LORRI will also be used to perform sensitive searches for potential satellites of the targeted bodies and any rings or dust associated with possible current or past surface activity. In addition to its use as a scientific imager, L'LORRI also serves as the primary optical navigation camera for *Lucy*, allowing early acquisition of the flyby targets and systematic monitoring during the approach phase to enable making accurate trajectory correction maneuvers to the flyby aim points.

In this paper, we describe L'LORRI's objectives, its design requirements that enable achieving those objectives, and the ground calibration results used to characterize its performance prior to launch. We also discuss how L'LORRI is used operationally during the *Lucy* mission, we outline the in-flight calibration plan that will be used to measure and trend L'LORRI's performance over the mission's lifetime, and we provide some results from L'LORRI observations taken during the first year of in-flight operations.

L'LORRI is the successor to the LORRI instrument on the *New Horizons* mission (Cheng et al. 2008; Weaver et al. 2020), which has continued to operate successfully in space for more than 17 years without any degradation in performance. L'LORRI essentially performs the same functions on the *Lucy* mission that LORRI has been performing on the *New Horizons* mission. However, there are some differences between L'LORRI and LORRI, which we describe here.

## 2 L'LORRI Objectives and Their Implementation

### 2.1 Science Objectives

The *Lucy* mission's scientific objectives and the spacecraft and instrument requirements necessary to achieve those objectives are summarized in NASA's Program Level Requirements Appendix (PLRA) for *Lucy*. The PLRA specifications relevant to L'LORRI for each Trojan flyby are:

- To support global imaging for shape models and the identification of geological units, obtain images spaced by 1/25 to 1/13 of a rotation over a full rotation period during the approach phase, and obtain images of the entire sunlit surface at a series of phase angles between 15° and 25° during the close encounter phase.
- To support stereo imaging for the creation of elevation models, obtain images of an area  $\geq 100 \text{ km}^2$  with sub-spacecraft resolution of  $\leq 200 \text{ m}$  at two emission angles.
- To enable the investigation of landform degradation at different latitudes, obtain images that cover an area  $\geq 500 \text{ km}^2$ , or 50% of the sunlit area, and regions from the equator to  $\geq 60^\circ$ , with characteristic resolution  $\leq 100 \text{ m}$ .
- To investigate the impact crater size distribution, obtain images that cover  $\geq 700 \text{ km}^2$ , or 80% of the sunlit surface, that can resolve craters  $\geq 7 \text{ km}$  across (i.e., cover the large end of the distribution), and obtain images that cover  $\geq 10 \text{ km}^2$  that are capable of resolving craters  $\geq 70 \text{ m}$  in diameter (i.e., cover the small end of the distribution).
- Search the region of stable satellite orbits to detect any bodies  $\geq 2 \text{ km}$  in diameter, assuming a geometric albedo  $\geq 0.04$ .

Each of the above PLRA specifications are flowed down to more refined requirements in the Lucy project “Mission Requirements Document” (MRD), which lays out the high-level requirements for the spacecraft subsystems and instruments. The MRD requirements in turn drive even more detailed requirements for each instrument, which must be implemented by the individual instrument teams and verified by the *Lucy* project.

To summarize, L'LORRI's main high-level objectives are: (1) obtain high-resolution images of the Trojan surfaces, (2) perform searches for satellites and dust around the Trojans, and (3) obtain the optical navigation images required to support spacecraft trajectory corrections. These are essentially identical to the objectives of *New Horizons* LORRI, except the targets were Pluto and its satellites rather than the Jovian Trojans. LORRI successfully achieved all of its objectives during the Pluto flyby, and L'LORRI's requirements have been tailored to ensure that its objectives can be met during the *Lucy* flybys.

## 2.2 Requirements

As an optical imaging system, L'LORRI is required to obtain high-resolution, panchromatic images under low light conditions. There are no requirements to perform multispectral imaging, which is handled by another instrument on the *Lucy* payload (Reuter et al. 2023). The driving requirements for the instrument involve resolution (point spread function, or PSF), signal-to-noise ratio (SNR), and environments. The key design requirements for L'LORRI are summarized in Table 1. Except where noted, all of these requirements were verified during the ground calibration campaign conducted at APL, with specific results discussed later in this paper.

The original LORRI instrument was designed to return high SNR imagery from Pluto at 33 au from the Sun, whereas L'LORRI's science targets have heliocentric distances in the range 5.2–5.7 au. Although the sunlight level at the Trojans is 30–40 $\times$  larger than at Pluto, *Lucy*'s Trojan targets have average albedos that are  $\sim 15\times$  smaller than Pluto's average albedo, so the surface brightness levels during the Trojan flybys might only be  $\sim 2\text{--}3\times$  larger than the Pluto surface brightness levels encountered during the *New Horizons* flyby. L'LORRI must be able to measure the brightest regions on the Trojans ( $I/F \sim 0.4$ ) without saturating and also support imaging of the darker Trojan surfaces at relatively high solar phase angles (down to  $I/F \sim 0.0014$ ). L'LORRI can achieve these objectives with a combination of high ( $\geq 3000$ ) instantaneous dynamic range and the use of two or more exposure times.

L'LORRI is a catadioptric telescope based on a Ritchey-Chrétien design, with hyperbolic-shaped primary and secondary mirrors made of silicon carbide, and a 3-element field-flattening lens assembly mounted in the hole of the primary mirror (Fig. 1). The photodetector consists of a frame transfer CCD detector with associated readout electronics. Table 2 provides a summary of the key characteristics of L'LORRI. The mass value (11.24 kg) includes the OTA (6.96 kg), the FPU (1.01 kg), the DPU (1.77 kg), all harnesses (0.72 kg), and all thermal blankets (0.78 kg). The power value (9.92 W) includes operational power for the FPU (2.11 W), operational power for the DPU (4.48 W), and the OTA operational heater power (3.33 W), but excludes the power drawn from the spacecraft-controlled decontamination heater to maintain the OTA at its specified value ( $\sim 2.3$  W).

L'LORRI is mounted on an instrument pointing platform (IPP) located outside the *Lucy* spacecraft (Fig. 2 and Fig. 3) and is exposed to more challenging environments than the original LORRI, which was mounted inside the *New Horizons* spacecraft. Unlike LORRI, L'LORRI is subjected to a highly variable thermal environment. The silicon carbide (SiC) optical telescope assembly (OTA) structure was supposed to mitigate any issues associated

**Table 1** Main L'LORRI instrument level requirements

ID	Requirement
LL-INST-3	The L'LORRI bandpass shall cover at a minimum 500 nm to 850 nm with a sensitivity over the entire range that is at least half the peak sensitivity within this range <sup>1</sup>
LL-INST-5	L'LORRI shall have a PSF with FWHM $\leq 15 \mu\text{rad}$ over the entire CCD <sup>2</sup>
LL-INST-7	The full FOV shall be $5.0 \text{ mrad} \pm 10\%$ , square
LL-INST-9	The instantaneous FOV (IFOV) shall be $4.94 \mu\text{rad} \pm 10\%$
LL-INST-11	L'LORRI shall have $\text{SNR} \geq 7$ for a point source with $V = 15.8$ in a single 10 s exposure in $4 \times 4$ mode with the PSF centered on a pixel
LL-INST-13	L'LORRI shall have $\text{SNR} \geq 6$ for a point source with $V = 15.2$ in a single 5 s exposure in $1 \times 1$ mode with the PSF centered on a pixel
LL-INST-15	L'LORRI shall have $\text{SNR} \geq 4$ for a point source with $V = 19$ in a series of 10 co-added images, each with a 10 s exposure in $4 \times 4$ mode with the PSF centered on a pixel
LL-INST-17	L'LORRI shall have $\text{SNR} \geq 25$ for a resolved target with $I/F=0.0014$ at a heliocentric distance of 5.7 au with a 100 ms exposure
LL-INST-19	L'LORRI shall have a point source transmittance (PST) for out-of-field stray light $\leq 0.02$ at angles $\geq 1 \text{ deg}$
LL-INST-21	L'LORRI shall have a dynamic range $\geq 3000$ in a single exposure
LL-INST-27	L'LORRI shall provide image data with an absolute radiometric accuracy of $\pm 10\%$ after application of a calibration routine
LL-INST-29	L'LORRI shall provide image data with a relative radiometric accuracy of $\pm 2\%$ from exposure to exposure and pixel to pixel
LL-INST-31	L'LORRI shall provide image data with a relative radiometric accuracy of $\pm 2\%$ from pixel to pixel within a single image

These instrument-level requirements flow down from higher level scientific requirements specified in the *Lucy* Mission Requirements Document (MRD), whose requirements in turn flow down from NASA's Program Level Requirements Appendix (PLRA) for the *Lucy* mission.

<sup>1</sup>A waiver was obtained in this case because the bandpass was reduced by design to mitigate artifacts from optical ghosts.

<sup>2</sup>This requirement was verified for the required FOV but not for the full CCD.

with the predicted large range of temperatures during the Trojan flybys ( $-75 \text{ C}$  to  $-125 \text{ C}$ ), but ground testing (see later discussion) showed that the optical performance degraded significantly as the temperature was lowered. A spacecraft-controlled contamination heater can be used to warm the L'LORRI OTA when necessary to improve the optical performance during science operations. L'LORRI is also required to withstand slightly higher radiation levels and have higher micrometeoroid impact survivability requirements compared to LORRI.

Although the launch vehicles for *New Horizons* (ATLAS V 551) and *Lucy* (ATLAS V 401) are similar, the launch load requirements for L'LORRI were set significantly higher than for LORRI, which meant that the L'LORRI OTA required a stronger mechanical structure. The exposure to external environments did relax requirements on accommodation of the CCD, as maintaining it at a cold temperature no longer required a radiator. During the approach to the Trojans, L'LORRI is required to image the Trojan surfaces at  $\text{SNR} \geq 25$  in a single image with an exposure time of 100 ms. The resolution requirement is to have a full-width half-maximum (FWHM) point spread function of  $\leq 15 \mu\text{rad}$  to obtain imagery of the Trojans sufficient to meet the science objectives after accounting for jitter from the spacecraft. Although most scientific imaging benefits from having the tightest possible PSF (i.e., the smallest possible FWHM), optical navigation objectives generally

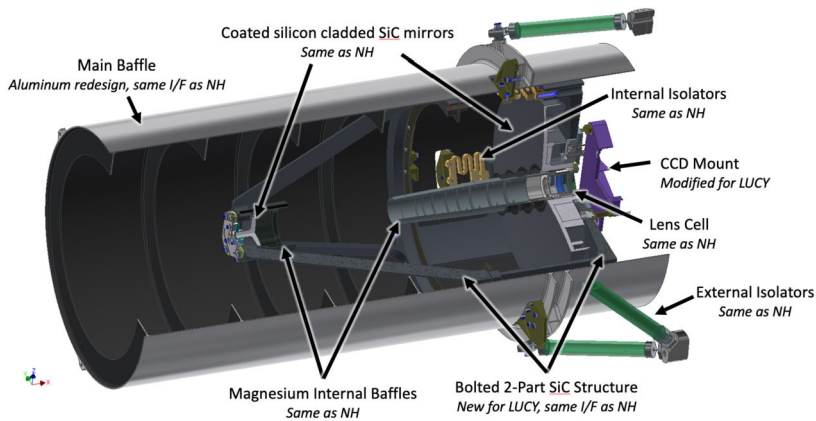


**Fig. 1** CAD drawing of L'LORRI showing its mechanical design and differences with *New Horizons* LORRI. Both telescopes have a Ritchey-Chrétien optical design and a 3-element field-flattening lens assembly mounted in the hole of the primary mirror. L'LORRI's main baffle and vanes were constructed from a single block of aluminum, while NH-LORRI has a baffle composed of a ceramic composite with aluminum vanes installed separately. L'LORRI's optical telescope assembly (OTA) structure is comprised of two separate silicon carbide pieces that are bolted together, whereas they were fused together for NH-LORRI. Both telescopes use essentially identical CCDs, but NH-LORRI's requires an attached radiator for cooling while L'LORRI's does not. Both telescopes have identical mechanical isolation systems (internal and external) to mitigate potential vibrational coupling to external environments that could degrade the optical performance. Here "I/F" is short for "interface"

benefit from having a broader PSF so that stellar images are not under sampled. L'LORRI is designed to meet imaging requirements at cold temperatures, with the OTA near  $-95$  C. At room temperature the performance is only required to be stable to allow for trending of performance under ambient laboratory conditions.

L'LORRI has a  $4 \times 4$  pixel binning mode, for which its limiting magnitude requirement is  $V \approx 19$ . The in-flight throughput measurements discussed later suggest that a single L'LORRI  $4 \times 4$  image with an exposure time of 64.9 s can achieve  $\text{SNR} \approx 5$  on a star having  $V \approx 21$  if there are few nearby stars (i.e., the background field is relatively sparse) and there is no solar scattered light.

### 2.3 Planned Observations

Each Trojan flyby is comprised of several phases (see Olkin et al. 2024 for a more extensive discussion of *Lucy* operations), all of which require L'LORRI activities:<sup>1</sup> Pre-Acquisition (E−300d to E−60d), Acquisition (E−60d to E−30d), Approach (E−30d to E−4d), Close Approach (E−4d to E+4d), and Departure (E+4d to E+20d). Even before pre-acquisition, during the so-called "cruise" phase, L'LORRI will observe the targeted Trojans roughly every year to investigate their phase behavior under geometrical conditions unavailable from Earth-based observatories, which will inform some details of L'LORRI's measurements (e.g., the selection of exposure times) during the later flybys.

During the pre-acquisition phase, the spacecraft subsystems and L'LORRI will be configured to enable the subsequent phases (e.g., set the appropriate thermal environment for L'LORRI). L'LORRI will perform systematic optical navigation ("OpNav") observations

<sup>1</sup>"E" is short for "Encounter" and "d" is short for "days"; thus, E−60d is short for 60 days before encounter.

**Table 2** Summary of L'LORRI key parameters

Item	Description
Optical Telescope Assembly (OTA)	L3H Ritchey-Chrétien optical design with 3-element field flattener lens assembly Silicon Carbide (SiC) structure, SiC mirrors coated with high reflectance dielectric 20.8 cm primary mirror diameter, $\sim 11\%$ central obscuration Focal length = 263.446 cm OTA in-flight operating temperature is approximately $-95\text{ C}$ No moving parts
Focal Plane Characteristics	Teledyne-e2v 47-20 frame transfer Charge Coupled Device (CCD) detector CCD frame transfer time $\approx 12\text{ ms}$ $1024 \times 1024$ optically active pixels, $13\text{ }\mu\text{m}$ square pixels AR-coated, backside-thinned, backside-illuminated CCD $1 \times 1$ and $4 \times 4$ (rebinned) output formats Field of View (FOV) = $505.190$ milliradians = $0.28946$ deg (square) Pixel FOV (IFOV, $1 \times 1$ format) = $4.9335\text{ }\mu\text{rad}$ = $1.0176$ arcsec (square) Correlated Double Sampling (CDS) with 12-bit Analog-to-Digital Converter (ADC) Full well $\approx 80,000\text{ e}$ (linear range) Anti-blooming technology to mitigate the effects of saturated targets in the FOV Electronics noise $\approx 19\text{ e}$ Dynamic range $\approx 3500$ (single image) Gain: $21.1\text{ e DN}^{-1}$ ( $1 \times 1$ ), $20.0\text{ e DN}^{-1}$ ( $4 \times 4$ ) Dark current $\leq 0.040\text{ e s}^{-1}\text{ pixel}^{-1}$ ( $1 \times 1$ at operating temperature of $-80\text{ C}$ ) Available exposure times: 0 ms to 64,900 ms at 1 ms spacings 1 Hz maximum frame rate (minimum time between consecutive images is 1 s)
Mass and Power	Total Mass = 11.24 kg; Power = 9.92 W
Wavelength Range	Panchromatic (no filters) with $\sim 63\%$ peak QE $420\text{--}795\text{ nm}$ at 50% of peak QE, $380\text{--}860\text{ nm}$ at 10% of peak QE
Photometric Accuracy	$\sim 2\%$ ( $1\sigma$ ) absolute for solar-type spectral energy distribution (SED) after in-flight calibration $\leq 10\%$ ( $1\sigma$ ) absolute for non-solar-type SEDs after in-flight calibration $\leq 1\%$ ( $1\sigma$ ) relative for signal-to-noise ratio (SNR) $\geq 100$

during the Acquisition and Approach phases at a cadence specified by the OpNav team to enable accurate spacecraft targeting to the designed aim point (i.e., miss distance from the Trojan). The OpNav imaging will be complemented by additional science imaging for better characterization of the Trojan's behavior (e.g., measure light curves for body shape determinations), perform observations of known satellites (e.g., Queta for Eurybates and the Patroclus-Menoetius binary), search for new satellites, and search for dust and other signs of Trojan activity.

The most scientifically interesting L'LORRI imaging will occur during a several hour period surrounding closest approach to the Trojan. At that time, the instrument pointing platform (IPP) will be commanded to point the L'LORRI boresight at the sub-spacecraft location on the Trojan. L'LORRI itself will be commanded into a special "noodle" mode in which the exposure time will alternate between short ( $\sim 15\text{ ms}$ ) and long ( $\sim 100\text{ ms}$ )

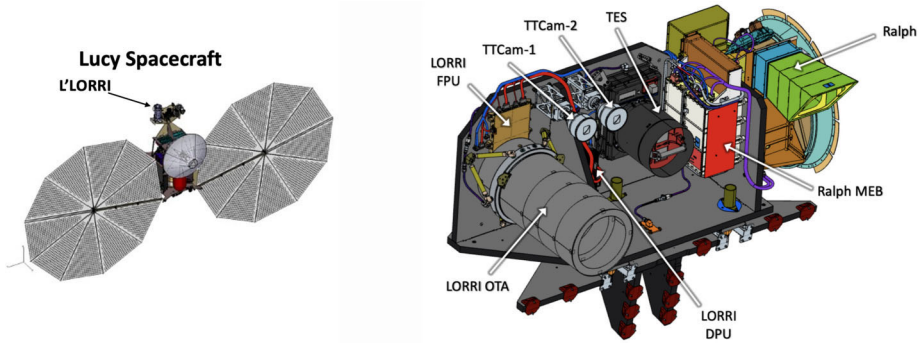


**Fig. 2** Left: Drawing of the *Lucy* spacecraft with its two large solar arrays, each of which is  $\sim 7$  m in diameter. L'LORRI and the other instruments are mounted on the instrument pointing platform (IPP), which stands off from the spacecraft and can be rotated in two orthogonal directions by two different gimbal mechanisms. Right: Magnified view of the IPP showing the locations of L'LORRI and the other instruments. "FPU" and "DPU" are the L'LORRI Focal Plane Unit and Data Processing Units, respectively. "MEB" is the L' Ralph electronics module

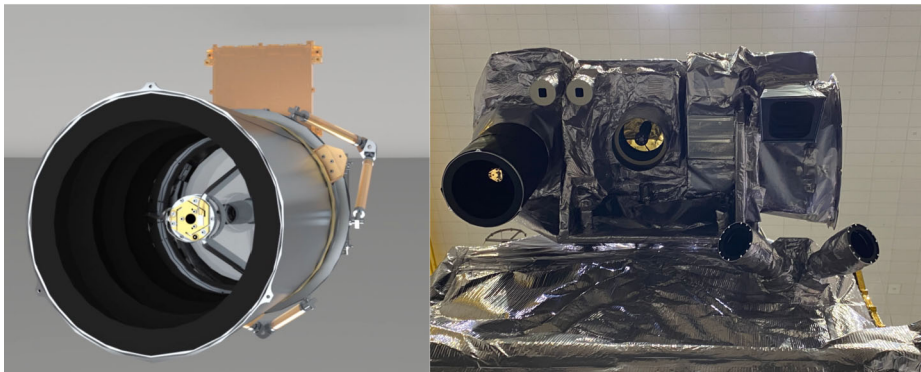


**Fig. 3** Left: CAD drawing of L'LORRI, not including its thermal blankets. The focal plane unit (FPU) is the brown box located behind the optical telescope assembly (OTA). Right: Photo showing all the *Lucy* mission instruments covered in thermal blankets and mounted on the instrument pointing platform (IPP), which itself is mounted on top of the spacecraft, shortly before the entire spacecraft was encapsulated within the launch vehicle fairing in September 2021. In addition to the components identified in Fig. 2, two orthogonally pointed star trackers are mounted on the spacecraft just below L' Ralph

exposure times every second to expand the dynamic range of the imaging and capture with high SNR both high and low reflectance regions on the Trojan surface, while minimizing image smear caused by Trojan surface rotation and relative motion during each exposure.

In addition to the scientific imaging during each encounter, L'LORRI will be exercised multiple times throughout the cruise phase to verify nominal functionality and perform calibration observations. The cruise phase data will enable systematic monitoring and trending of L'LORRI's performance over the full mission duration. This includes detailed in-flight characterization of L'LORRI's point spread function (PSF) during observations of star clusters, investigation of optical ghosts by observing bright stars, investigating solar scattered light in different observational geometries (especially under conditions mimicking the Trojan flyby geometry), and measuring the absolute sensitivity by observing a solar-type ab-

solute calibration standard star. Near the time when the first Earth Gravity Assist (EGA1) was performed in October 2022, we executed extensive observations of the Moon's surface, which tested L'LORRI's ability to measure craters with sub-PSF resolution using deconvolution techniques, similar to what is planned for measuring the Trojan crater size distributions during those flybys (Robbins et al. 2023a,b).

Subject to *Lucy* mission budget and operational constraints, various "cruise science" L'LORRI observations will be conducted that will enhance the mission's scientific return beyond its baseline activities, which are focused on the initial spacecraft investigations of the Jovian Trojan population.

## 3 Instrument Description

### 3.1 Overview

The L'LORRI instrument development was led by The Johns Hopkins University Applied Physics Laboratory (JHU-APL, or APL for short) with many of the original LORRI staff reprising their roles on L'LORRI after almost two decades. Integration and test (I&T) efforts began in the spring of 2020 and coincided with the outbreak of the COVID-19 pandemic, which presented significant logistical and safety challenges to the team throughout the entire I&T campaign, as well as after delivery of the instrument to the spacecraft. Despite these challenges, L'LORRI was delivered to the *Lucy* spacecraft in late-October 2020, it exhibited nominal performance during the subsequent ground testing, and it was launched into space on the *Lucy* spacecraft in October 2021.

L'LORRI has three sub-assemblies in close proximity connected by electrical harnesses. These are the Optical Telescope Assembly (OTA), which was manufactured by L3-Harris SSG (L3H), the focal plane unit (FPU), and the data processing unit (DPU). L'LORRI has two DPUs for redundancy, and either DPU can be used with either of two spacecraft command and data handling (CDH) computers (cross-strapping). The baseline plan is to use only one of the DPUs for the entire mission, with the second DPU only being powered for periodic functional testing (cold redundancy). All components are mounted to the instrument pointing platform (IPP) on the spacecraft (Fig. 2). Unlike LORRI, L'LORRI does not have an aperture door because the contamination risk was judged by the *Lucy* project to be smaller than the risk of a door opening failure.

L'LORRI is electronically shuttered and has no moving parts. The OTA focuses light onto a Charge Coupled Device (CCD; model 47-20 supplied by Teledyne-e2v), which is part of the FPU. The CCD is a  $1024 \times 1024$  pixel (optically active region), back-thinned, backside-illuminated device that incorporates anti-blooming technology to eliminate bleeding of the electrons along columns when bright targets saturate (i.e., when the signal in a pixel exceeds the full-well capacity of  $\sim 80,000$  electrons). The FPU contains a single electronics board connected to the CCD.

For the highest resolution observations, all optically active pixels are read out from the CCD ("1×1" format) with a square IFOV (individual pixel field-of-view) of  $1.0'' \text{ pixel}^{-1}$  and a square FOV of  $1024'' \times 1024''$ . The pixels can also be re-binned by a factor of 4 in each direction (i.e., column and row directions) during CCD readout ("4×4" format), which reduces the data volume by a factor of 16, increases the SNR because the readout noise is added only once for 16 pixels, and results in an IFOV of  $(4.0'' \text{ pixel}^{-1})$  but with the same FOV. During readout in either format, the analog signals are processed using correlated



double-sampling (CDS) and converted to 12-bit data numbers (DNs) using an analog-to-digital converter (ADC; only 12 bits of a 14-bit device are used), yielding a valid DN integer range from 0 to 4095. The digitized image is then transferred to flash memory in the DPU (see below).

Whenever L'LORRI is active, the CCD is exposed to whatever scene is in the FOV. The clocking of the CCD includes a "frame scrub", followed by exposure to the scene for the commanded integration time, followed by a "frame transfer" in which the CCD rows are sequentially transferred from the optically active area to the image storage region, followed by a readout of the image storage region to the downstream electronics. Owing to the finite transfer time, photons from the source continue to be integrated during the fast image shift, thereby producing the so-called transfer smear. However, as long as the source is not saturated, transfer smear can be effectively and deterministically removed during post-processing at the cost of some additional photon noise. Unlike the case for LORRI, the L'LORRI scrub and transfer times are exactly equal (11.7762 ms), which considerably simplifies the algorithm used to remove the smear transfer signal in the calibration pipeline.

L'LORRI does not have any color filters. Instead, L'LORRI maximizes sensitivity by providing panchromatic imaging over a wide bandpass: 420–795 nm at the 50% throughput points. Image exposure times range from 0 ms to 64,900 ms in 1 ms increments. Images can be taken at a maximum rate of once per second, or at any commanded cadence longer than that.

A flexible autoexposure mode is available whenever the scene being imaged has unknown intensities, but autoexposure can only be used for exposure times  $\leq 900$  ms. Although we plan to check the autoexposure capability during in-flight L'LORRI functional tests, we don't currently have plans to use this mode in-flight, except possibly during observations to characterize solar scattered light. When making in-flight L'LORRI observations of a target with unknown, or poorly characterized, brightness, we will usually opt to use two different *manual* exposure times that span the dynamic range of interest, rather than relying on autoexposure mode.

A "trigger" mode is also available that enables L'LORRI to determine autonomously when a target has entered the FOV, via analysis of a 32-bin histogram of the image, and then run an onboard macro routine that saves images to the flash memory for a specified cadence and duration after the trigger condition has been satisfied. We do not anticipate using trigger mode during any of the Trojan flybys, but we successfully tested it during L'LORRI observations of the Moon near the time of the first Earth gravity assist (EGA-1). Trigger mode functionality is also routinely tested in-flight using the L'LORRI internal lamps.

Each DPU has 64 Gb of flash memory, which can store over 4400  $1 \times 1$  format images, which is much larger than the expected number of images collected during any single Trojan flyby ( $\sim 2000$   $1 \times 1$  images). Although there is room in flash memory to store over 70 thousand  $4 \times 4$  format images, the total number of images stored in either format is limited by flight software design to a maximum of 11,264, which is the number of possible entries in the onboard image allocation table. The images stored in the DPU's flash memory can be transferred by command to the spacecraft's command and data handling (CDH) computer, which losslessly compresses them to its solid state memory as part of the transfer process. The spacecraft can send selected images to its telecommunications hardware for downlink to the antennas of NASA's deep space network (DSN). The DPU handles all L'LORRI communications with the spacecraft.

The spacecraft controls several survival heaters situated throughout the instrument, as well as a decontamination heater, which is used to warm the optics during all science activities. The L'LORRI DPU controls several operational heaters that are used to maintain

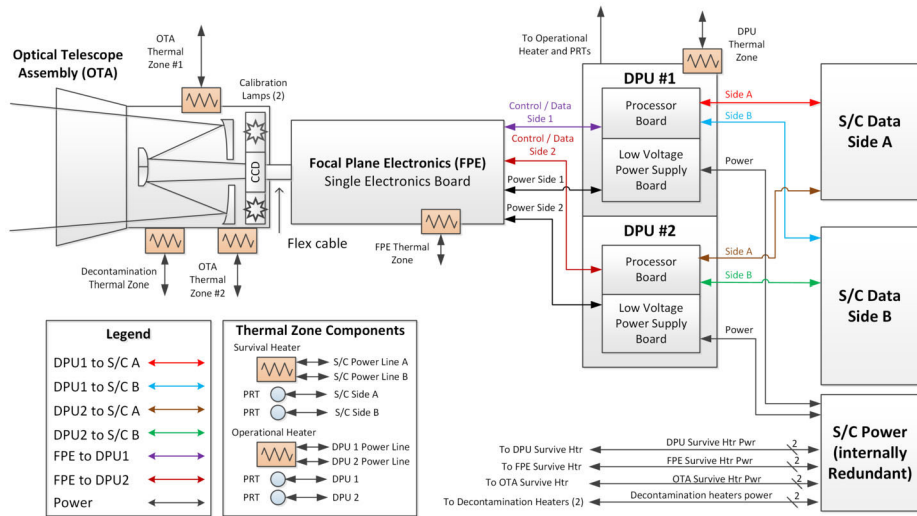


Fig. 4 L'LORRI block diagram showing the major components of the instrument and its interfaces to the *Lucy* spacecraft

instrument temperatures within acceptable ranges during operations. Figure 4 is a block diagram of L'LORRI showing the main instrument components.

### 3.2 Design Requirements and Trades

The stringent optical, thermal, and structural requirements for the original *New Horizons* LORRI OTA presented many design challenges, with maintenance of high resolution without the need for focus adjustments as the primary driver. This led to the use of Silicon Carbide (SiC) for the structure and reflective optics, which, in principle, would allow for operation over the wide thermal range expected during the different *Lucy* Trojan flybys. Thus, the L'LORRI OTA uses the same basic design as LORRI with a few exceptions. The higher design launch loads for *Lucy* required additional mass in the OTA structure for more strength. The primary baffle material changed from a composite to aluminum, which is cheaper and can be manufactured quicker. The bandpass was optimized to reduce ghosting, while still maintaining sufficient signal to meet performance requirements. LORRI was mounted inside the *New Horizons* spacecraft, and a radiator was needed to cool the LORRI CCD down to its specified operating temperature (approximately  $-80$  C). But this radiator was deleted from the L'LORRI design because L'LORRI is mounted to the Instrument Pointing Platform (IPP), which is open to cold space allowing passive cooling of the CCD to its desired operating temperature (also near  $-80$  C).

The L'LORRI electronics required significant redesign as requirements in general for electronics have changed significantly over the last two decades. New controls and quality requirements as well as additional radiation requirements, including Enhanced Low Dose Rate Sensitivity (ELDRS) testing, was needed. The thermal blankets around the OTA were changed to a less reflective material to reduce reflections into other instruments. Several of the major trades for L'LORRI centered on reducing mass, which had strict requirements during the design phase. This included changing the material of the DPU housing from aluminum to magnesium for mass reduction.

### 3.3 Optical Design

The L'LORRI OTA is a Ritchey-Chrétien design with an emphasis on high system throughput to measure Trojan dark surfaces at high phase angles, search for faint satellites near the main bodies, and assist with optical navigation. Since the *Lucy* science objectives for L'LORRI were so similar to the LORRI objectives on *New Horizons*, L'LORRI adopted essentially the same optical design as LORRI. During the last two decades, there has been an evolution in the techniques L3H uses to manufacture and process SiC optics, and most of the L'LORRI OTA components benefitted from those innovations. However, the spare primary mirror (M1) from the *New Horizons* LORRI program became the M1 for L'LORRI because an error was discovered during the final processing of the newly manufactured L'LORRI M1 mirror and schedule pressure precluded waiting for a new M1 to be produced and tested before the *Lucy* launch. The unintended variation of focus with temperature discovered during the ground testing of L'LORRI (discussed in more detail later) may be related to the use of the original LORRI M1 in the L'LORRI OTA, but there is no direct evidence to support that hypothesis.

The complete L'LORRI OTA design was evaluated with a Structural, Thermal, and Optical Performance (STOP) analysis. This included time-dependent analysis during both the approach and departure phases associated with the Trojan flybys. Fortunately, the OTA thermal environment changes insignificantly during the few hours centered on closest approach owing to the OTA's high thermal inertia. Stray light was modeled in FRED, a commercial optical analysis software package.

### 3.4 Thermal Design

The L'LORRI thermal environment posed a design challenge relative to the heritage case. LORRI was mounted within the interior of the *New Horizons* spacecraft, and the OTA temperature has been passively maintained near  $-80$  C throughout the entire mission. In contrast, the L'LORRI is mounted outside the *Lucy* spacecraft with predicted OTA temperatures ranging from  $-120$  C to  $-75$  C for different Trojan flybys, assuming there is no active thermal control. The design challenge was to minimize defocus due to thermal gradients arising in the L'LORRI OTA metering structure.

The main OTA structure was manufactured using SiC 55a to produce a nearly athermal design that enables passive operation. The high conductivity of SiC acts to minimize thermal gradients, and SiC's low coefficient of thermal expansion minimizes the thermal strain impact of such gradients. Invar 36, a good match to SiC 55a over the temperature range of interest, was chosen for the metallic inserts that allow bolting together of the OTA assembly to improve its strength. All invar inserts, as well as the secondary mirror foot, were epoxy bonded to the SiC.

The OTA is mounted inside the telescope baffle tube, which is made of aluminum. The baffle tube provides a relatively uniform cold sink along the length of the telescope that helps to reduce longitudinal thermal gradients. The telescope is mounted to the spacecraft via long G-10 isolators, which isolate the OTA conductively from the spacecraft deck. The entire OTA (except for the entrance aperture) is covered with multilayer insulation (MLI), which minimizes radiative coupling between the OTA and space. The secondary mirror is mounted to a flexured Invar 36 plate, which in turn mounts to the end of the SiC metering structure. The secondary and primary mirror magnesium baffles are flexure mounted to the OTA structure (SiC) and the lens cell (Invar 36), respectively. The CCD mount plate is attached to the OTA structure by titanium flexures, which serve the dual purpose of mitigating

thermal strain and thermally isolating the CCD from the structure. The G-10 mounts for the overall OTA have titanium post flexures on either end. Additionally, the OTA itself is mounted to the aluminum baffle tube via titanium isolators, which act to mitigate thermal strain and vibrations and to provide conductive isolation.

The baseline mission design ran the decontamination heaters with setpoints of  $-10\text{ C}$  for the first six months of the mission to promote early desorption of water vapor and at  $-40\text{ C}$  for the rest of the mission (except during science or optical navigation operations when the OTA is kept cooler) to mitigate against potential condensation of volatiles. The CCD must be maintained at a temperature colder than  $-70\text{ C}$  while acquiring science data to achieve acceptable levels of dark current. This requirement is met passively from cooling by the OTA, which balances the heat transfer from the FPU that generally runs at a warmer temperature.

The L'LORRI in-flight temperatures were predicted via a finite difference thermal model that included all conductive and radiative heat transfer. A thermal balance test of the instrument was performed that validated the thermal model, and a separate thermal balance test was performed at the spacecraft level to further validate the model.

The STOP analysis for the different encounter geometries demonstrated that a passive design produced minimal gradients in the OTA metering structure. Optical performance with the expected gradients was included in the final performance analysis and was within the performance specification on resolution. However, ground testing showed that the OTA focus varied significantly with temperature and slightly violated the resolution requirement at the coldest temperatures. Thus, we decided to re-purpose the spacecraft-controlled decontamination heater to force the OTA to a temperature near  $-95\text{ C}$  for all science observations. This new strategy should produce similar optical performance for all L'LORRI imaging, including all of the *Lucy* mission flybys.

### 3.5 Mechanical Design

The structural design objectives of the OTA were to minimize mass while maintaining performance over operational temperatures and allowing for the stiffest design that will survive the launch environment. The requirements were a maximum mass of 7.3 kg, a minimum resonant frequency of 60 Hz, and survival under launch-induced vibration and stresses. The inherently high stiffness-to-weight ratio of SiC ( $\sim 4.5$  times that of aluminum) allowed the fabrication of a low-mass structure with a light-weighted primary mirror of open back, hub-mounted design to minimize weight (identical to the original LORRI).

The main baffle tube, including its vanes, was fabricated from a single block of aluminum. The smaller internal baffles were fabricated from a light-weight magnesium alloy (ZK60A). Vibration isolation was required to survive the launch environment. Titanium isolators were incorporated to mount the structure to the main baffle tube at three points approximately at its center of gravity location. Another important structural design consideration was to minimize any potential for mount-induced distortion of the optics. Intimately connected to this design consideration is the requirement for the OTA to mount to a surface with only moderate mounting coplanarity, namely, a spacecraft honeycomb panel. To avoid degradation of optical quality, a three-point mount was adopted, with the bases of each of the three mount locations on the OTA outfitted with a ball joint that can be loosened and re-tightened, if necessary. At the interface between the main baffle tube and the OTA inner assembly, the vibration isolators also act to mitigate any mount-induced strains. The flexurized mount plate at the secondary mirror serves the dual purpose of controlling thermally induced distortions, as well as mount-induced distortions; the CCD flexure mounts

also serve this dual purpose. Due to its mass, the primary mirror was not flexure-mounted, as the low resultant frequency and dynamic responses would have increased the risk to the OTA under vibration. Instead, the primary mirror is hub-mounted, with a post and a foot bolted via three invar inserts to a mount plate. The mount plate is in turn bolted to the structure. Because the lens cell is made of Invar and mounts to the structure, close to the primary mirror, the mount plate helps to separate any induced thermal strain in the structure from being transferred to the primary mirror.

### 3.6 Instrument Integration, Focus, and Alignment

When the OTA was assembled at L3H, a convex spherical reflector was centered at the focus using interferometry. Metrology, combined with knowledge of the shim size used to connect the reflector to the carrier plate, determined the location of the focus relative to the interface location on the carrier plate. L3H also provided a reference mirror on the back of the secondary mirror mount, such that the telescope line-of-sight was parallel to the reference mirror's normal. Two optical reference flats at right angles to the line-of-sight were mounted to the L'LORRI metering structure for use in alignment monitoring after mounting to the spacecraft.

The depth of focus for L'LORRI at the detector, with mechanical tolerances on the CCD, allowed initial shim sizes to be selected for system focusing at the L3H-provided focus location. A 300-mm aperture,  $f/5$  off-axis parabolic collimator was used to project a point-like image into L'LORRI. This image was produced by a laser unequal path interferometer (LUPI) at the collimator focus. A series of exposures were made at several points in the L'LORRI field by moving within the field using a fold mirror. At each location, the spot was centered on a detector element by viewing the live image from the CCD through ground support electronics, and balancing the wings of the image symmetrically about the center detector element. This was repeated for several focus adjustments of the collimator, with slight measured changes from nominal to allow for deterministic shimming of L'LORRI. Data from these exposures were examined to find the best L'LORRI focus versus the collimator adjustment. New shims were then installed to move the plane of the CCD onto the plane of best focus. Once at nominal focus, the CCD was centered on the optical axis by use of a theodolite viewing both the reference mirror on the back of the secondary mount and the primary mirror. The theodolite was auto-collimated on the reference mirror, and the azimuth and elevation recorded. The theodolite then viewed the four corners of the CCD off the primary mirror, and these azimuth and elevation values were recorded and averaged. The CCD location was shifted in the plane of best focus such that the average of the four CCD corners was within tolerance of the normal to the reference mirror.

After the best focus was found in ambient conditions, L'LORRI was installed in the APL optical calibration facility (OCF) for a focus check at flight-like thermal and vacuum conditions. This was done by viewing a collimated beam, which projected a small point-like image into L'LORRI, and stepping the spot over the field by tilting L'LORRI on a gimbal platform.

Prior to delivery to the spacecraft, L'LORRI's line-of-sight was measured relative to the optical reference flat mounted to the back of the secondary mirror support. Additionally, the roll angle was measured by viewing the CCD corners, and referencing to the orthogonal alignment mirrors. These data, combined with measurements performed referencing the flats to the spacecraft coordinate system, showed that L'LORRI's line-of-sight was within mission requirements. Tracking of the L'LORRI alignment references through the spacecraft environmental test program did not show any significant movement relative to the spacecraft coordinate system.

**Table 3** L'LORRI Contamination Requirements

Component	Requirement
External Surfaces	400 A/2
Internal Surfaces	250 A/2
CCD	350 A/2

These requirements refer to beginning-of-life values for the *Lucy* mission (i.e., valid at launch). Requirements refer either to Particulate or Non-Volatile Residue (molecular) contamination.

### 3.7 Contamination Control

The L'LORRI telescope assembly remained under a nitrogen purge during all phases of integration and test until launch, except for limited times when images were taken or when put under vacuum. The internal cleanliness requirements for the L'LORRI OTA per the L'LORRI specification are given in Table 3. The outgassing of the entire instrument was verified to be below  $5 \times 10^{-12}$  g cm<sup>-2</sup> s<sup>-1</sup> during thermal vacuum testing at the highest survival temperatures allowed for the instrument.

### 3.8 Electronics

As shown in Fig. 4, the L'LORRI electronics consist of the DPU and FPU. The DPU contains two printed circuit cards: the low-voltage power supply (LVPS), and the processor board (PB). The DPU is the primary interface between the spacecraft and the FPU, which is directly connected to and controls the CCD. There are two DPUs to provide redundancy; either DPU can be used with either of two redundant spacecraft CDH computers. Only one DPU side is active at a time; the other is a cold spare.

#### 3.8.1 FPU

The L'LORRI FPU is required to read out a complete image in one second, with the charge level in each pixel represented by a 12-bit binary word. The FPU noise is required to be <40 electrons per pixel, well above the CCD read noise, which is calculated to be about 10 electrons at the readout time of about 0.7 μs per pixel. In general, exposures of 20 to 200 ms are typical for L'LORRI science images, although bias images are taken with the minimum commanded exposure time of 0 ms, the maximum exposure time is 64.9 s, and optical navigation images typically use 5 s and 10 s exposure images.

The FPU also includes two small incandescent bulbs mounted on the same sub-board as the CCD. These lamps can illuminate the CCD via light scattered off the back end of the OTA structure (Fig. 5), so that testing can be performed even when imaging is not possible through the optics (e.g., functional testing). These lamps were from the same batch of lamps as the original *New Horizons* LORRI, which produced output light levels that have been stable to ~1% for the entire (ongoing) mission. The illumination pattern produced by the lamps provides a means of testing whether there has been any change in the relative pixel response over the entire CCD, including whether there has been any change in any foreign object debris (FOD) on the CCD (see Sect. 4.2.7).

The L'LORRI CCD uses a three-phase architecture for charge transfer in the image, memory zone, and serial registers. For optimum performance, these phases must be clocked

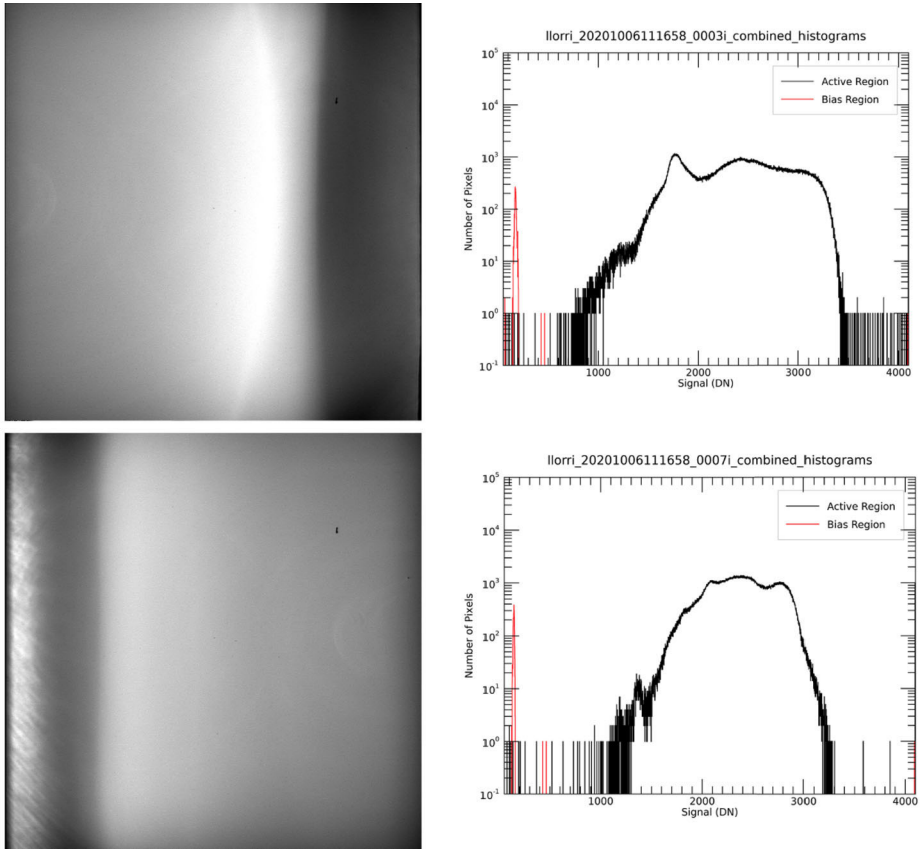


**Fig. 5** Top left: An image from internal lamp 1. Top right: Histogram of the image from lamp 1. Bottom left: An image from internal lamp 2. Bottom right: Histogram of the image from lamp 2. Both images are displayed on a linear scale spanning 1000 DN to 3500 DN. Both lamps were set to a level of 100, and the image exposure time was 100 ms

with specific waveforms and voltage levels. These phase lines are highly capacitive, particularly for the image and memory areas of the chip, and they experience mutual capacitive coupling. L'LORRI uses drivers that are designed to drive high capacitance loads at the required voltage levels from logic level inputs. They are switching, not linear, devices so that low and high voltage levels are obtained by a suitable choice of supply voltages, and transition rates must be adjusted at the output. This is done with series resistance, which adds to the internal switch resistance of the drivers, forming a simple time constant with the capacitance of the CCD phase.

The CCD requires 29 V bias for the output field effect transistor. A charge pump with pre- and post-regulation was used to generate this voltage. The L'LORRI FPU uses an integrated circuit that performs correlated double sampling, signal amplification, and analog to digital conversion to 12 bits (after dropping the two least significant bits of the 14-bit ADC) at maximum rates of 6 MHz, comfortably above the pixel readout rates, which are  $\sim 1.5$  MHz. The integrated double sampling circuit is potentially susceptible to latch-up from ionizing radiation and heavy particle impact in space, therefore the L'LORRI FPU incorporates latch-up protection circuitry that was tested in proton irradiation facilities.

### 3.8.2 DPUs

The L'LORRI processor board (PB) controls the instrument via interfaces to the LVPS board. The PB communicates to the spacecraft using an RS-422 link, which receives commands and transmits engineering data. The PB uses an FPGA processor and runs FORTH code. There are dual, redundant interfaces on the spacecraft, which provide command, data handling, and telemetry functions. One interface is active and one is a back-up; L'LORRI provides both interfaces (low voltage differential signal, or LVDS, for high-speed image data and RS-422 for low-speed command and telemetry) to both sides of the spacecraft. Secondary functions of the L'LORRI PB include the ability to:

- Store and transmit the image and header information
- Calculate a 32-bin histogram
- Generate test patterns without an FPU present
- Command the FPU mode and exposure times

The PB can generate test pattern images without an FPU present. The first pattern consists of a horizontal ramp, and the second pattern consists of a vertical ramp. The imager interface FPGA can also receive data from the spacecraft once a second, and those data are used to set the FPU mode and exposure time. The instrument engineering data are transmitted by the spacecraft within a separate data stream from the science data, and the engineering data must be associated with individual images in ground processing. However, the critical header information is encoded into the images themselves, at the cost of 56 pixels in the first row of each image. The FPGA also calculates a 32-bin histogram of the FPU image data currently being transmitted. This histogram is then made available to the instrument for future exposure time calculations (e.g., for AUTO exposure mode). The FPGA collects the FPU status and temperature data, making it available to the instrument for thermal control purposes. The LVPS provides power at the voltage required by the other boards within the DPU and by the FPU. The input voltage from the spacecraft is 24–34 V. The LVPS board provides switching to control power on/off to the FPU and the instrument operational heaters.

The 64 Gb of flash memory resides on the DPU PB. When images are taken, they are written sequentially to flash memory, where they can be retrieved non-sequentially by spacecraft command using either the observation identification number (OBSID), which is set by a L'LORRI command, or by memory index number, which is managed by the L'LORRI flight software. L'LORRI images are typically transferred from flash memory to the spacecraft CDH memory within a second, but the CDH flight software also losslessly compresses each image and formats it for downlink as part of the transfer process, which typically takes ~23 s for each image. Additional image transfers are not allowed until the previous processing has been completed. The flash memory can be erased by L'LORRI command, typically after verification that the previously stored data have been successfully downlinked to Earth. Note that the flash memory in one DPU cannot be accessed by the other DPU. That is, the two flash storage devices, like the DPUs themselves, are completely independent of each other.

### 3.8.3 Flight Software

The L'LORRI processor shares a common design with that of many instruments that APL has flown. This common design extends to the software. The common flight software (CFS) provides packet telemetry and command handling services. Besides handling L'LORRI-specific packets, the CFS automatically generates a variety of standard packets, including



housekeeping and status, command echo, memory dump, and alarm packets. Similarly, besides handling L'LORRI-specific commands, the CFS also handles standard commands for memory loads and memory dump requests. The CFS also provides storage and execution of command sequences.

The CFS has timekeeping, voltage and current monitoring, and memory management services, and a standard boot program. The L'LORRI-specific flight software controls heaters, collects voltages, currents, and temperatures from the LVPS board, and manages the FPU. In the FPU, the software controls the exposure time, either by manual command or automatically based on the hardware-provided image histogram, generates an image header, and enables routing of the image to the flash memory and then to the spacecraft. The software also controls the FPU's test patterns and internal lamps.

## 4 Ground Calibration Results

L3H delivered the flight model (FM) L'LORRI OTA to APL on 2020 April 14. L'LORRI underwent extensive ground testing at APL starting in May 2020 and ending with shipment to the *Lucy* mission spacecraft facility at Lockheed-Martin (LM) in Littleton, Colorado in late-October 2020. In this section, we describe the results from the ground testing at APL, which served to characterize L'LORRI and verify that it met its requirements. The testing at LM verified that L'LORRI's performance on the spacecraft was generally consistent with the results from the ground testing at APL, so we won't explicitly discuss the LM test results here.

The L'LORRI ground tests at APL are summarized in Table 4. Some of the early tests, including the pre-environmental calibration, were performed with the engineering model (EM) FPU and EM DPU because the flight models (FMs) were not yet available. However, the entire FM system was used during environmental testing in September 2020, and during the post-environmental calibration conducted in October 2020. No changes were made to L'LORRI after the post-environmental calibration.

The L'LORRI optical performance tests at APL were generally conducted either in a cleanroom, or in an adjacent optical calibration facility (OCF). L'LORRI in-flight conditions were simulated in the OCF (Fig. 6), and measurements in that facility during the post-environmental calibration were the most critical ones for verifying conformance with L'LORRI's requirements. Thus, we will mainly focus here on the results from the post-environmental calibration, except for results on optical ghosts, scattered light, and CCD saturation from measurements made in the APL cleanroom under ambient laboratory conditions.

For the OCF tests, L'LORRI was mounted on a rotation stage inside a thermal vacuum (TVAC) chamber. For PSF and focus measurements, L'LORRI was pointed at the output of a collimator mounted just outside a large (40.6 cm diameter) TVAC chamber window. The collimator has an off-axis, confocal Cassegrain design with a focal length of 1866 mm, an exit pupil of 304 mm (L'LORRI's entrance pupil is 208 mm), and a fold mirror that can scan across a  $1.1^\circ \times 2.4^\circ$  field (L'LORRI's field of view is  $0.29^\circ$ ). The pinhole in the collimator could be precisely moved along the optical axis to produce focus curves, that is, PSF measurements as a function of focus location along the L'LORRI optical axis. The collimator provided both broad bandpass (panchromatic) light, as well as light from a spectrograph to measure L'LORRI's spectral response (i.e., sensitivity as a function of wavelength).

L'LORRI could also be rotated to view a calibrated integrating sphere through a second 40.6 cm diameter window for flat-field and linearity measurements. Two different lamps

**Table 4** L'LORRI ground tests

Test ID	Timeframe (2020)	Comments
Special Early Tests	May	Measure scattered light and characterize optical ghosts. Also characterize amplifier undershoot/overshoot. All of this testing used the FM OTA but with an EM FPU and an EM DPU. All measurements made in APL cleanroom under ambient conditions with red (632 nm) laser illumination from a LUPI.
Preliminary Focus	Late-May and June	Preliminary focus characterization using the FM OTA, EM FPU, and EM DPU. Tests conducted in both the APL cleanroom under ambient conditions and in the OCF under flight-like conditions.
Pre-Environmental Calibration	June 27–July 8	Calibration measurements in flight-like environments with the FM FPU and EM DPU.
Thermal Cycle/Balance	September 5-17	Mostly performed to verify thermal models but included the best measurements of bias and readnoise, including their variations with temperature.
Post-Environmental Calibration	October 1-7	Calibration measurements in flight-like environments with the FM FPU and the FM DPU.
ATLO TVAC	May 2021	L'LORRI testing while integrated on the <i>Lucy</i> spacecraft.

EM refers to an Engineering Model, and FM refers to the Flight Model. OTA stands for the Optical Telescope Assembly. LUPI is a Laser Unequal Path Interferometer. OCF refers to the APL Optical Calibration Facility. ATLO stands for Assembly, Test, and Launch Operations. TVAC refers to testing in a Thermal Vacuum chamber under flight-like conditions. All tests were conducted in 2020, except for ATLO TVAC.

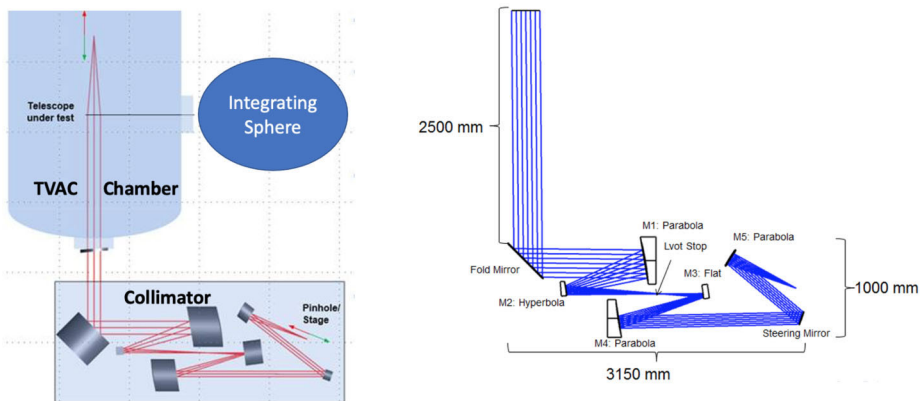


**Fig. 6** Left: Drawing of the APL optical calibration facility (OCF), where the main L'LORRI ground calibration was conducted. L'LORRI was placed in the thermal vacuum (TVAC) chamber. Point Spread Function (PSF) and focus measurements were conducted by illuminating L'LORRI through a large window in the TVAC chamber using the collimator located just outside the TVAC chamber. L'LORRI could also be rotated to view an integrating sphere through a second window for flat-field and linearity measurements. Right: Ray trace showing the collimator optical path

were used to illuminate the integrating sphere: a plasma discharge lamp provided a reasonably good approximation to the solar spectrum for most of the visible light portion of the spectrum, while a quartz halogen lamp was used to mimic the solar spectrum at the longer

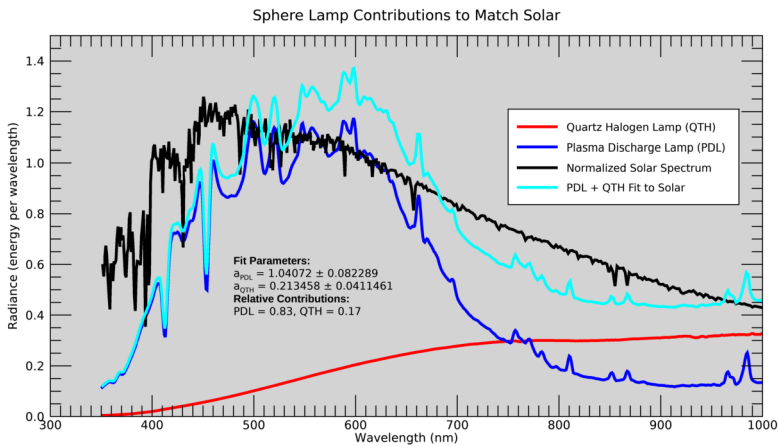


**Fig. 7** The solar spectrum is compared to the spectra of the two lamps used to illuminate the integrating sphere during the L'LORRI calibration measurements. The linear combination of the two lamp spectra that provides the best fit to the solar spectrum is also displayed. To produce the best fit, the plasma discharge lamp has a weighting factor of 0.83 and the quartz halogen lamp has a weighting factor of 0.17, which are the weighting factors used to produce the final L'LORRI flat field

wavelengths. The relative spectral distributions of each lamp, and the linear combination that best matches the solar spectrum, are displayed in Fig. 7.

## 4.1 Optical Performance

We first discuss the optical performance, which includes:

- Focus variation with temperature
- Point spread function (PSF) quality and encircled energy (EE)
- Scattered light
- Ghosts

### 4.1.1 Focus Variation

Contrary to its design specification, the L'LORRI OTA is *not* athermal, as demonstrated by testing at both L3H and APL. Figure 8 shows that the L'LORRI focus location changes by up to 750  $\mu\text{m}$  over the full range of operating temperatures (i.e., from +20 C to -125 C). As previously discussed, the change in focus with temperature motivated us to use the spacecraft-controlled decontamination heater to force the L'LORRI OTA temperature to be near -85 C for all science observations. As discussed in Sect. 5, preliminary in-flight testing suggests that an even colder OTA temperature (near -95 C) produces better optical performance. In any case, up to  $\sim 2.3$  W of extra power is required to heat the OTA to the desired temperature during in-flight operations, which is available from a spacecraft-controlled decontamination heater.

The location of the L'LORRI CCD relative to the best focus position has a relatively large uncertainty of  $\pm 100$   $\mu\text{m}$ . Based on the post-environmental calibration data, our best estimates for the L'LORRI focus locations as a function of OTA temperature are depicted in Fig. 9. At the originally targeted OTA temperature of -85 C, the OTA best focus may lie up to  $\sim 400$   $\mu\text{m}$  in front of the CCD, or the best focus may be only  $\sim 200$   $\mu\text{m}$  in front of

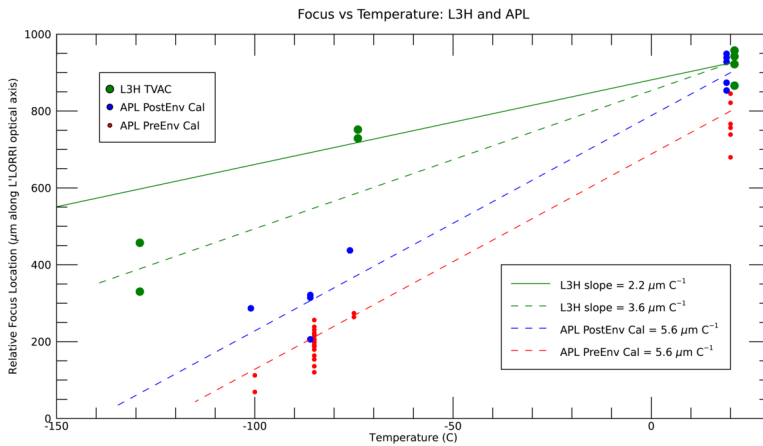


**Fig. 8** Plot showing focus versus temperature results for the on-axis location for both L3H and APL measurements. The uncertainty in the focus location appears to be about  $\pm 100 \mu\text{m}$  for both sets of data. The APL data seem to show a steeper change in focus location with temperature, but both data sets show a large change in focus location as the OTA is cooled to the temperature expected for the *Lucy* mission science observations (probably close to  $-95 \text{ C}$ )

**L'LORRI Focus Locations: Post-Environmental Results**

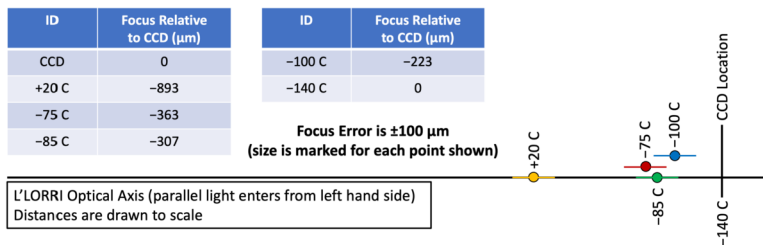


**Fig. 9** Figure showing the estimated L'LORRI focus locations relative to the CCD location for various temperatures based on the post-environmental ground calibration measurements. The uncertainties in the focus locations are  $\pm 100 \mu\text{m}$ . For the *Lucy* mission science and optical navigation observations, the OTA will be thermostatically controlled to a temperature near  $-95 \text{ C}$ , with the final thermal set point determined after more in-flight tests are conducted

the CCD. Fortunately, the focus curve for the L'LORRI OTA is relatively flat, and the PSF quality only degrades modestly when moving off best focus (see Sect. 4.1.2).

**4.1.2 PSF Quality and Encircled Energy (EE)**

During testing at APL, we performed focus runs comprised of the following activities:

- Rotate the collimator beam in altitude and azimuth to position it at 13 locations across the L'LORRI FOV
- At each FOV location, drive the collimator focus stage through 17 different positions (i.e., motions of the image along the L'LORRI optical axis), approximately  $\pm 8$  locations about the optimal focus position, using more closely spaced positions near nominal focus to enable better fitting of the focus curve

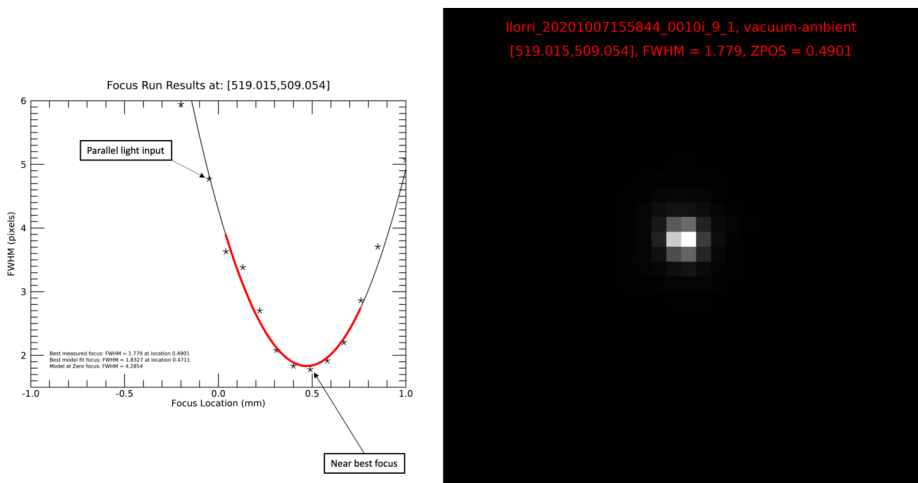


**Fig. 10** Left: Focus curve for the OTA at room temperature (+20 C) near the center of the CCD. The curve is relatively sharp with the PSF FWHM depending strongly on the focus location. Right: PSF near the best focus location, which is relatively symmetrical with a FWHM of 1.8 pixels. The display uses a linear stretch grayscale ranging from the minimum to maximum values of the PSF

- Take 3 images at 1 second cadence at each piston location using an exposure time of 10 ms

L'LORRI has  $\sim 1$  arcsec pixels, which imposes severe constraints on the quality and stability of the collimator image. The APL OCF facility was commissioned only shortly before the start of the L'LORRI ground calibration campaign, and the L'LORRI team had to troubleshoot multiple issues that arose during the course of this testing. In particular, the team struggled to control environmental factors that affected collimator image stability (e.g., not allowing anyone in the collimator room during optical testing, turning off vacuum pumps, turning off thermal control fans, etc.; image stability was affected by both the collimator stability and the stability of L'LORRI's mounting fixture within the OCF thermal vacuum chamber). Despite using extremely short L'LORRI exposure times, the collimator image motion was typically at least 1-2 L'LORRI pixels during each image. Thus, the PSFs measured during our testing at APL are generally degraded relative to their true quality. The image quality was judged by fitting an elliptical Gaussian to the PSF and quoting the geometrical mean of the major and minor axis diameters as the "FWHM". L'LORRI has a requirement that the PSF must have  $\text{FWHM} \leq 3$  pixels over most of the CCD. The "encircled energy" (EE), defined as the ratio of the signal contained within the peak pixel relative to the signal integrated over the entire PSF, is another measure of image quality. L'LORRI must have  $\text{EE} \geq 0.04$  (i.e.,  $\text{EE} \geq 4\%$ ) to meet its most challenging SNR requirement.

The L'LORRI PSF has a sharp focus curve and a tight PSF ( $\text{FWHM} \leq 2$  pixels) (best fit Gaussian) at room temperature (Fig. 10). The PSF is roughly circularly symmetric, and the EE is  $\sim 20\%$  over much of the field at best focus (Fig. 11). However, EE decreases to  $\sim 5\%$  for the out-of-focus PSF at the location where the CCD is mounted when parallel light is sent into the L'LORRI OTA under room temperature conditions.

The L'LORRI PSF monotonically degrades in quality as the temperature is lowered, mainly a result of increasing astigmatism with decreasing temperature. This behavior was neither expected (i.e., not consistent with the specification), nor has it been successfully

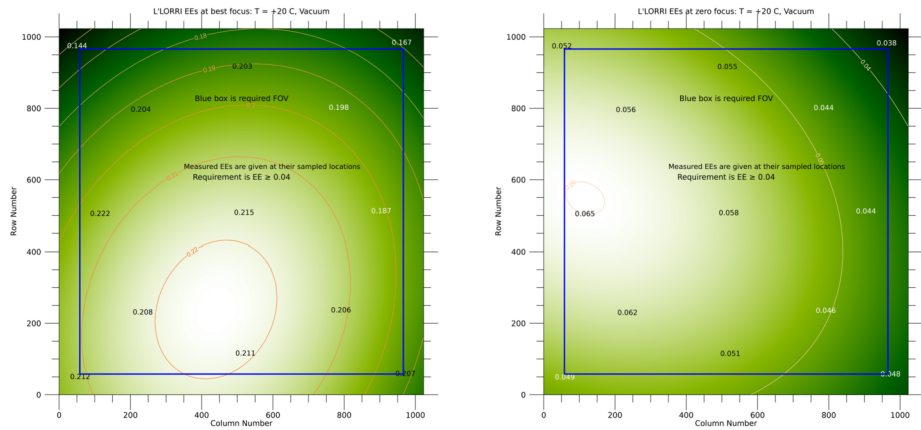


**Fig. 11** Left: EE values across the CCD at best focus when the OTA is at room temperature (+20 C). The color background image is created by fitting a 2-dimensional polynomial of degree 2 to the measured EE values (at the positions indicated on the image) and is displayed using a linear stretch ranging from the minimum to maximum EE values. Smaller EE values are darker green, and larger EE values are lighter green. The EE values are  $\sim 20\%$  across most of the CCD. Right: The same but with parallel light input to the OTA, which is focused  $\sim 900\ \mu\text{m}$  in front of the CCD (see Fig. 9). The EE values are  $\sim 5\%$  across most of the CCD

modeled by L3H. Given the change in focus with temperature and the degradation in image quality at lower temperatures, we decided to use the spacecraft-controlled decontamination heater to fix the OTA temperature at the predicted OTA temperature for the “warmest” Trojan flyby ( $-85\ \text{C}$ ) for *all* L'ORRI science and optical navigation observations, rather than allow the OTA temperature to vary over the large range predicted for the different Trojan flybys ( $-85\ \text{C}$  to  $-120\ \text{C}$ ). We also tried to put the CCD at the best focus location for an OTA temperature of  $-85\ \text{C}$ , but that was not completely successful (see Sect. 4.1.1) owing to discrepancies between focus data taken in the APL cleanroom (which we used to shim the CCD location) and data taken in the APL OCF.

Despite these difficulties, L'ORRI still meets its *Lucy* mission requirement over the required FOV when the OTA temperature is  $-85\ \text{C}$ . Figure 12 shows the focus curve at  $-85\ \text{C}$ , which is much flatter than the curve at room temperature, and therefore more forgiving in focus location. The FWHM is expected to be in the range 2.5–2.7 pixels over the FOV (Fig. 13), and the EE should be  $\sim 9\%$  over the FOV (Fig. 14). The in-focus PSF at  $-85\ \text{C}$  is more symmetrical than the out-of-focus PSF, but the FWHMs are comparable (Fig. 15).

We note that the PSFs from the ground calibration were degraded by image instability, and we expected the in-flight performance to be better, assuming spacecraft jitter didn't significantly degrade the in-flight PSF. Although the initial in-flight testing showed that spacecraft jitter didn't compromise the PSF for exposure times shorter than about 10 s, the PSF was slightly degraded relative to our expectations when the OTA was near  $-85\ \text{C}$ , causing us to consider operating the OTA at a colder temperature during L'ORRI science observations. See Sect. 5 for further discussion.

### 4.1.3 Scattered Light

The scattered light properties of L'ORRI were quantified by obtaining point source transmittance (PST) measurements in the APL cleanroom. This involved measuring L'ORRI's

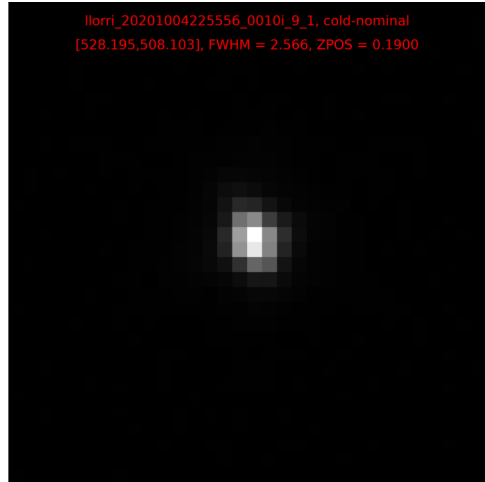
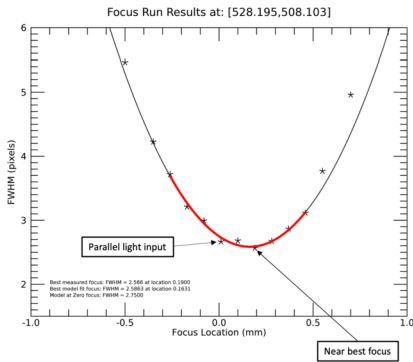


**Fig. 12** Left: Focus curve for the OTA at  $-85\text{ C}$  near the center of the CCD. The curve is relatively flat with the PSF FWHM changing only moderately with the focus location. Right: PSF near the best focus location, which has  $\text{FWHM} \approx 2.6$  pixels. The display uses a linear stretch grayscale ranging from the minimum to maximum values of the PSF

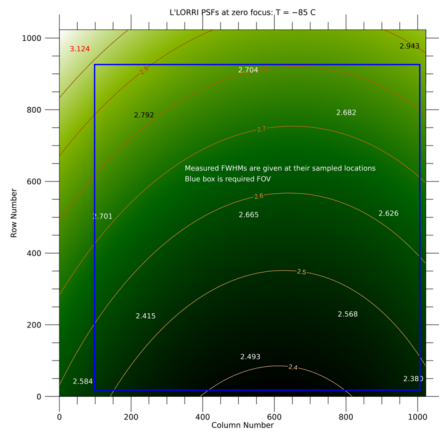
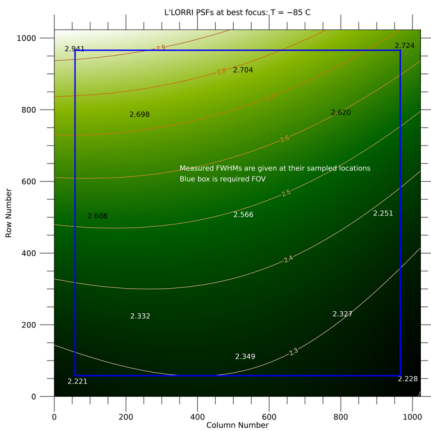


**Fig. 13** Left:FWHM values across the CCD at best focus when the OTA is at  $-85\text{ C}$ , which we targeted as the OTA temperature for all *Lucy* mission observations prior to launch. The color background image is created by fitting a 2-dimensional polynomial of degree 2 to the measured FWHM values (at the positions indicated on the image) and is displayed using a linear stretch ranging from the minimum to maximum FWHM values. Smaller FWHM values are darker green, and larger FWHM values are lighter green. The FWHM values are  $\sim 2.2\text{-}2.7$  across the CCD. Right: The same but with parallel light input to the OTA, which is focused  $\sim 300\text{ }\mu\text{m}$  in front of the CCD (see Fig. 9). The FWHM values are  $\sim 2.4\text{-}2.9$  across the CCD

response to point source illumination as a function of offset angle from the boresight (Fig. 16). The L’LORRI PST appears to be similar to the LORRI PST, which is expected given that both instruments have essentially identical optical designs. We originally hoped that the aluminum baffle used for L’LORRI, rather than the composite baffle used for LORRI, might reduce the scattered light for L’LORRI. But both baffles have aluminum vanes coated with Z306 black paint, and scattering from those surfaces is apparently dom-

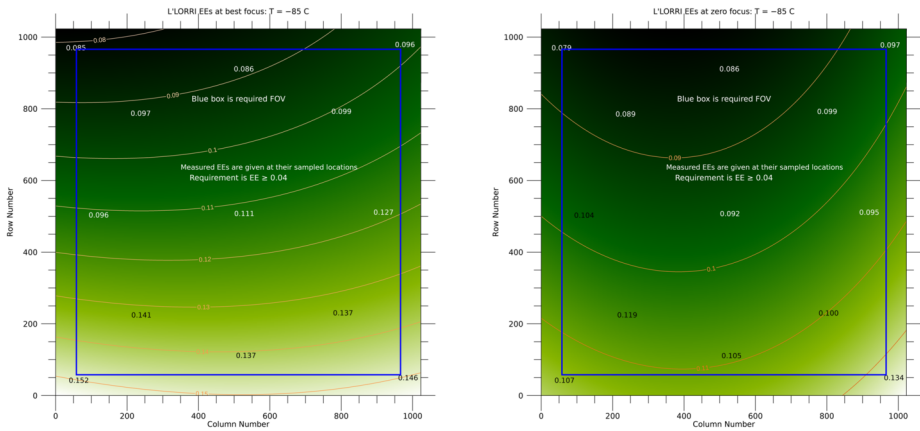


**Fig. 14** Left: EE values across the CCD at best focus when the OTA is at  $-85\text{ C}$ , the pre-launch targeted OTA temperature for all *Lucy* mission observations. The color background image is created by fitting a 2-dimensional polynomial of degree 2 to the measured EE values (at the positions indicated on the image) and is displayed using a linear stretch ranging from the minimum to maximum EE values. Smaller EE values are darker green, and larger EE values are lighter green. The EE values are  $\sim 11\%$  near the center of the CCD. Right: The same but with parallel light input to the OTA, which is focused  $\sim 300\ \mu\text{m}$  in front of the CCD (see Fig. 9). The EE values are  $\sim 9\%$  near the center of the CCD

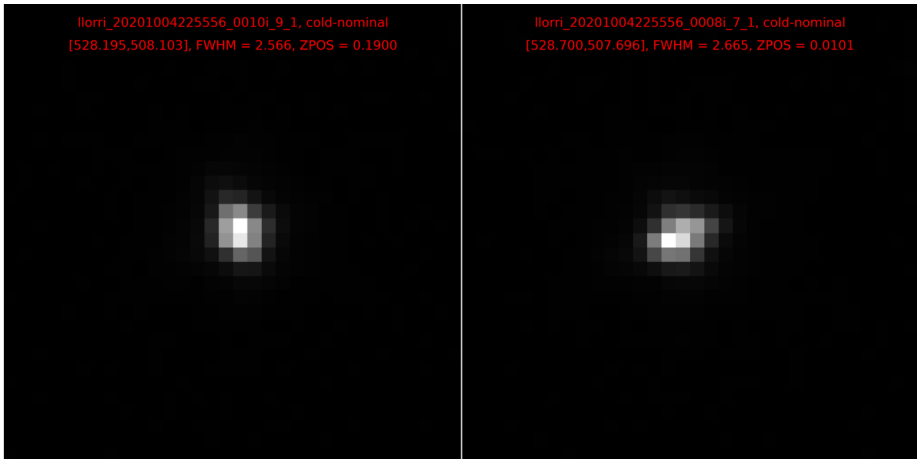


**Fig. 15** Comparison of the PSF near the center of the CCD at  $-85\text{ C}$  for best focus (left) and for parallel light input to the OTA when the CCD is  $\sim 300\ \mu\text{m}$  behind the best focus. The best focus case is more symmetrical, but both PSFs have similar FWHMs. Both images are displayed using a linear grayscale ranging from the smallest to largest values in the PSF

inant in producing the measured PST values. The Ritchey-Chrétien optical design used for both instruments, with its central obscuration, limits how well scattered light can be suppressed. Nevertheless, L'LORRI meets its scattered light requirement with significant margin.



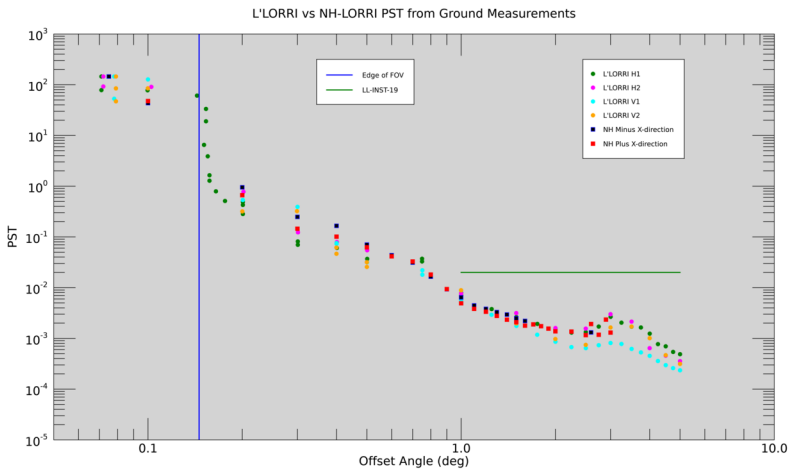


**Fig. 16** The point source transmittance (PST) is plotted for both LORRI and L'LORRI. In both cases, the input illumination was provided by red (632 nm) laser light. Four different scan directions were obtained for L'LORRI, and two scan directions were obtained for LORRI. The clump of points plotted between offset angles of  $0.07^\circ$  and  $0.08^\circ$  actually refer to an offset angle of  $0^\circ$  but are separated in the plot for better visibility. The PST curves for LORRI and L'LORRI are similar, as expected since they have essentially identical optical designs. L'LORRI easily meets its scattered light performance requirement (LL-INST-19)

#### 4.1.4 Ghosts

The L'LORRI optical design includes an assembly with three lenses mounted inside the hole in the primary mirror (M1). The purpose of the lens assembly is to flatten the image plane, which would otherwise be significantly curved across the full extent of the CCD. Unfortunately, however, the lenses produce ghosts from multiple reflections within the assembly, which manifest as pupil images on the CCD (see Fig. 17 for an example). If the lenses are labeled by L1, L2, and L3 in order of increasing distance from the OTA secondary mirror (M2), and the two surfaces of each lens are labeled by S1 and S2 (with S1 being the surface closer to M2), the four ghosts marked in Fig. 17 are produced by internal reflections from the surfaces listed in Table 5.

The ghost with the highest surface brightness is A, which is almost twice as bright as B. For wavelengths near the middle of L'LORRI's bandpass, the integral of the ghost signal in A is roughly  $4 \times 10^{-4}$  times the integral over the PSF of the illumination source. The surface brightness in A is roughly  $3 \times 10^{-6}$  times the peak signal from the illumination source. Thus, for example, a  $V = 6.2$  star located just outside the L'LORRI FOV can produce a ghost whose surface brightness is approximately equal to the peak brightness of a  $V = 20$  star in the L'LORRI FOV. The presence of optical ghosts produced by nearby bright objects should be considered when planning L'LORRI observations, but no ghosts are produced for objects more than  $0.37^\circ$  from the L'LORRI boresight. Ghosts of similar morphology and brightness were also observed for *New Horizons* LORRI (Cheng et al. 2010).

## 4.2 Detector Performance

### 4.2.1 Bias

As is typical for CCDs, an electronic bias offset is applied to the CCD signal to prevent negative values at the analog-to-digital chip (ADC) that converts electrons to data numbers

**Fig. 17** Image showing ghosts produced by a bright point source located just outside the L'LORRI field of view (FOV). The four brightest ghosts are produced by multiple reflections within the field flattening lens assembly, as described in Table 5. For this image, the input light illumination was produced by a diode laser with a wavelength of 635 nm. The image is displayed using an ASINH stretch ranging from  $-10$  DN to 3835 DN

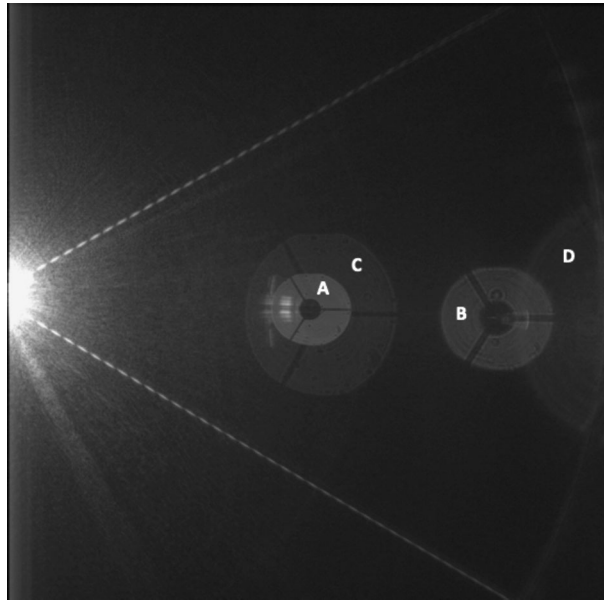


**Table 5** L'LORRI optical ghosts

Ghost ID	Surface Reflections Producing the Ghosts
A	L3S2 to L3S1
B	L3S1 to L2S2
C	L3S1 to L2S1
D	L3S2 to L1S1

Ghost IDs refer to the labels marked in Fig. 17. The nomenclature for the internal surface reflections that produce the ghosts is discussed in the body of the paper.

(DNs). In the L'LORRI calibration pipeline, the removal of this bias is a two step process: first, a global bias level is removed based on the average signal level for pixels sampled from the optically inactive region of the CCD, and then the pixel-to-pixel bias variation is removed using a so-called *superbias* image, which has a median level of 0 DN. Figure 18 shows the superbias image for  $1 \times 1$  format, and Fig. 19 shows the superbias image for  $4 \times 4$  format. In both cases, the bias levels in the lowest rows differ significantly from the bias levels in the rest of the image because there is a surge in current during the initial image-to-storage transfer that temporarily shifts the bias level.

For  $1 \times 1$  format images, four columns in the inactive region are captured, which means a total of 4096 pixels ( $1024 \times 4$ ) are used to compute a robust average of the global bias level. For  $4 \times 4$  format images, two columns in the inactive region are captured, which means a total of 512 rebinned pixels ( $256 \times 2$ ) are used to compute a robust average of the global bias level. However, there is a systematic offset between the bias level in the active and inactive regions of the CCD (Fig. 20), which is likely associated with different capacitive effects in the active and shielded regions of the CCD. The offset is 3.2 DN for  $1 \times 1$  images and 5.1 DN for  $4 \times 4$  images. The L'LORRI calibration pipeline accounts for this offset.

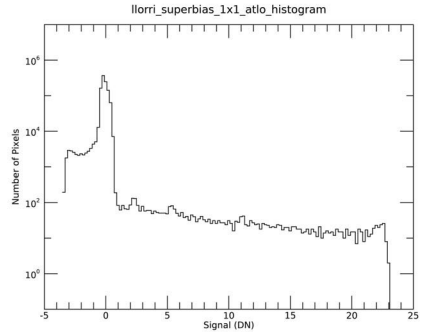
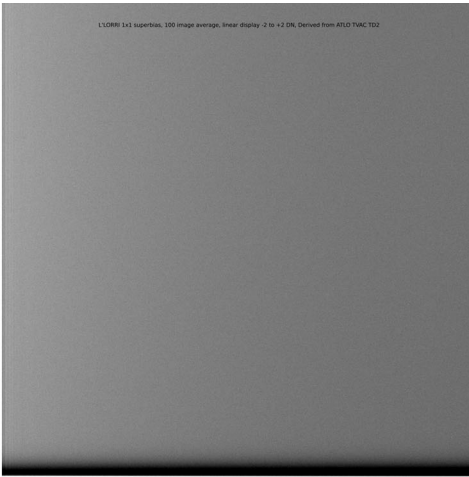


**Fig. 18** Left: Mean of 100 1 × 1 bias images ( $t_{exp} = 0$  ms), which is called a *superbias* image. The serial output amplifier is closest to the pixel at the bottom left of the image. Right: Histogram of the superbias image. The positive tail is associated with the lowest rows of the image, and the negative tail is associated with the rows just above them

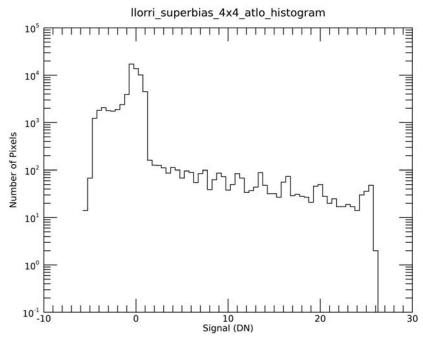


**Fig. 19** Left: Mean of 100 4 × 4 bias images ( $t_{exp} = 0$  ms), which is called a *superbias* image. Right: Histogram of the superbias image. The positive tail is associated with the lowest rows of the image, and the negative tail is associated with the rows just above them

For LORRI images, the bias level was a linear function of the temperature of the FPU board, with the bias level increasing by  $\sim 1.2$  DN for every 1 C change in the board temperature. In contrast, for L'LORRI images the bias level is essentially constant over the entire predicted temperature range of the FPU board during *Lucy* operations (Fig. 21).

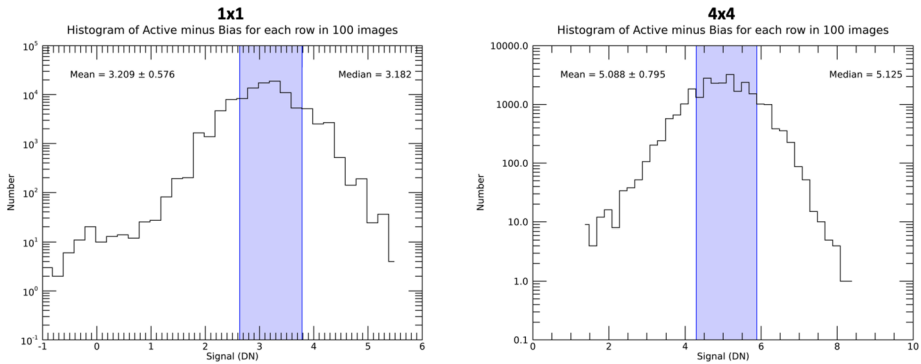
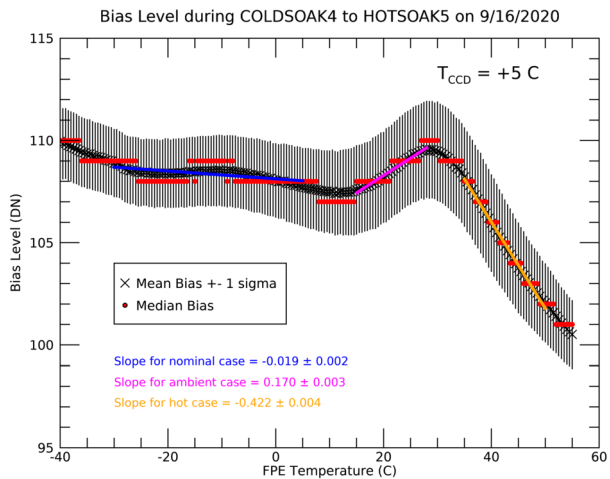


**Fig. 20** Histograms showing the offset in bias level between the active and inactive regions of the L'LORRI CCD: the robust mean for the bias region was subtracted from the robust mean for the active region for each row in each of  $100\ 1 \times 1$  images and  $100\ 4 \times 4$  images. The exposure time was 0 ms for all the images. The shaded regions show  $\pm 1\sigma$  about the mean differences. The mean of the active region is 3.2 DN larger than the mean of the bias region for  $1 \times 1$  images and 5.1 DN larger for  $4 \times 4$  images. See the text for further discussion

**Fig. 21** L'LORRI CCD bias level as a function of FPU board temperature, obtained during thermal cycle measurements at APL. The FPU board temperature is predicted to lie in the range  $-29\text{ C}$  to  $+4\text{ C}$  for *Lucy* observations, where the bias level is essentially constant. The CCD temperature was relatively high ( $+5\text{ C}$ ) for these measurements, which affects the global bias level but should not affect the variation with FPU temperature



### 4.2.2 Electronics Noise

The difference of two bias images ( $t_{exp} = 0$  ms) is analyzed to produce L'LORRI noise histograms. Following the technique outlined by Janesick (2001), we randomly sample  $25 \times 25$  pixel subarrays ( $7 \times 7$  pixel subarrays for  $4 \times 4$  format images) of the difference image for 50,000 randomly selected regions across the entire CCD to obtain a histogram of noise values, which includes the CCD read noise and any other noise introduced by the downstream electronics. Noise pickup from a thermal control rack compromised the measurements taken during the pre- and post-environmental testing, but the environment was much quieter during thermal cycle/balance testing, which provided an opportunity to measure the true L'LORRI system electronics noise. An example is shown in Fig. 22, which has both a noise histogram and a plot showing the variation of the noise with CCD temperature. For the temperatures relevant for the *Lucy* mission, the L'LORRI noise is well below the re-

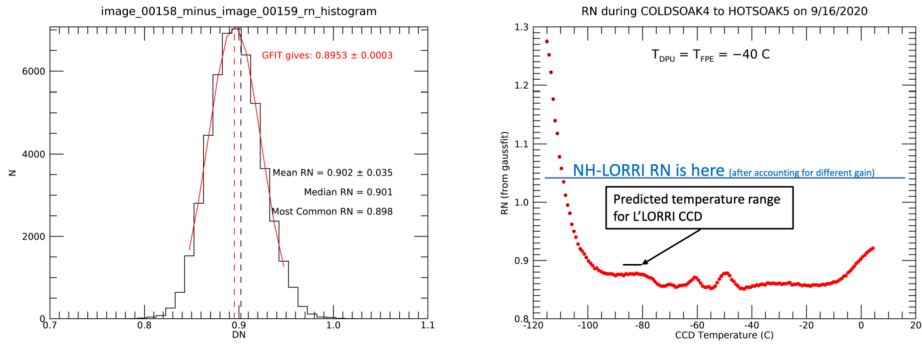


**Fig. 22** Left: L’LORRI noise histogram at a CCD temperature of  $-83\text{ C}$ , which is within the range predicted for in-flight conditions. The noise is  $\sim 0.9\text{ DN}$ , which is well below the requirement of  $1.9\text{ DN}$ . Right: Plot showing the variation of noise with CCD temperature. The temperature range predicted for in-flight conditions is indicated, as is the noise value measured for *New Horizons* LORRI

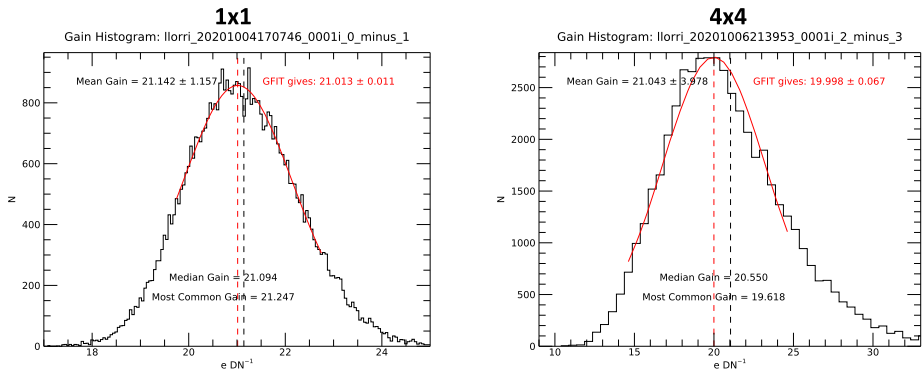


**Fig. 23** Gain histograms for  $1 \times 1$  format (left) and  $4 \times 4$  format (right). The gain for  $1 \times 1$  images is  $\sim 21.0\text{ e DN}^{-1}$ , and the gain for  $4 \times 4$  images is  $\sim 20.0\text{ e DN}^{-1}$

quirement ( $0.9\text{ DN}$  measured vs  $1.9\text{ DN}$  requirement) and is also significantly smaller than the value measured for *New Horizons* LORRI.

### 4.2.3 Gain

The electronics gain, which is the scale factor that enables conversion from electrons detected to DN, is slightly different for  $1 \times 1$  versus  $4 \times 4$  images. Again, we follow the technique outlined by Janesick (2001) to produce a gain histogram for each of the two CCD formats using two well-exposed images with essentially constant illumination over the entire CCD. We use differences of two flat field images taken from the post-environmental calibration conducted in October 2020. Examples of gain histograms are shown in Fig. 23. The gain for  $1 \times 1$  images ( $\sim 21.1\text{ e DN}^{-1}$ ) is slightly smaller than the gain for  $4 \times 4$  images ( $\sim 20.0\text{ e DN}^{-1}$ ).

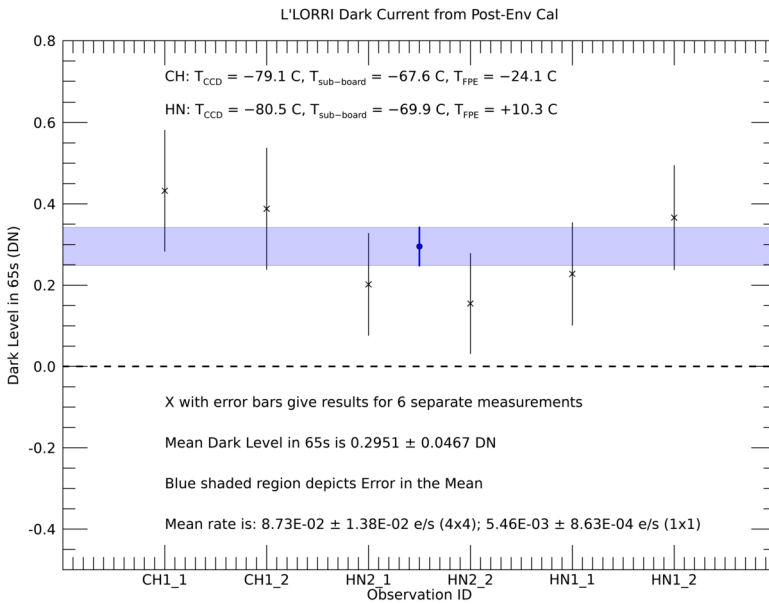


**Fig. 24** Dark current measurements from the post-environmental calibration at APL are plotted for two different thermal environments for the electronics, but with the CCD near  $-80 \text{ C}$  in all cases. The measured dark current is extremely low, comparable to that measured in-flight for *New Horizons* LORRI. See the text for further discussion

#### 4.2.4 Dark Current

At the predicted in-flight CCD temperatures, the dark current is expected to be essentially negligible. Nevertheless, we attempted to measure the dark current under flight-like conditions during the post-environmental calibration at APL. By taking three consecutive pairs of 0 ms and 64,900 ms images in  $4 \times 4$  format, and then subtracting the shorter exposure image from the longer exposure image, we were able to measure the dark current accumulation rate even when the CCD was cold. We performed measurements with L'LORRI in two different thermal environments: one with cold electronics and hot OTA ("CH" case) and one with hot electronics and nominal temperature OTA ("HN" case). In both cases, the CCD temperature was approximately  $-80 \text{ C}$ . Measurements were taken with both DPUs in the HN case ("HN1" for DPU1 and "HN2" for DPU2). Only pixels in the optically-inactive region of the CCD were used to avoid contamination from any residual background light. The results are displayed in Fig. 24 and demonstrate that the dark current from the L'LORRI CCD is extremely small, comparable to that measured for *New Horizons* LORRI.

#### 4.2.5 Linearity and Dynamic Range

Linearity and dynamic range were characterized by pointing L'LORRI at an integrating sphere and taking a series of images with different exposure times while the lamp intensity was held constant. By definition, the dynamic range refers to the maximum net signal level (after subtraction of the bias) in the linear response portion of a single exposure divided by the electronics noise (0.9 DN). The results presented here, which demonstrate that L'LORRI's response is linear to within  $\sim 1\%$  and the dynamic range for a single exposure is  $\geq 4200$ , are independent of which L'LORRI DPU side was used for the measurements.

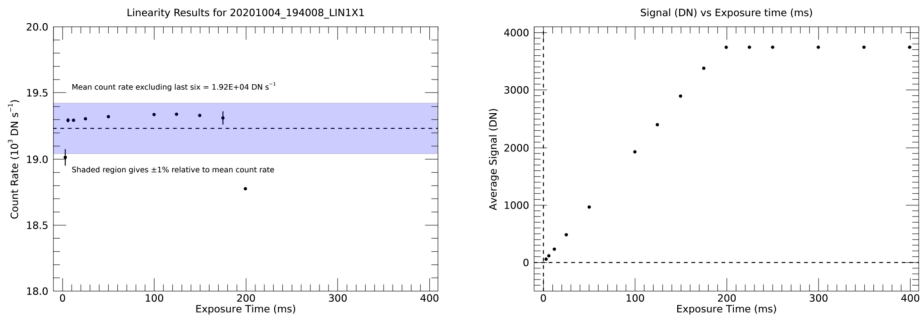


**Fig. 25** The plot on the left shows that the measured count rate for 1 × 1 images is within 1% of the mean value for all exposure times (the blue shaded region), except for the saturated ones. The plot on the right shows that the response remains linear up to at least a net signal level of 3400 DN after bias subtraction

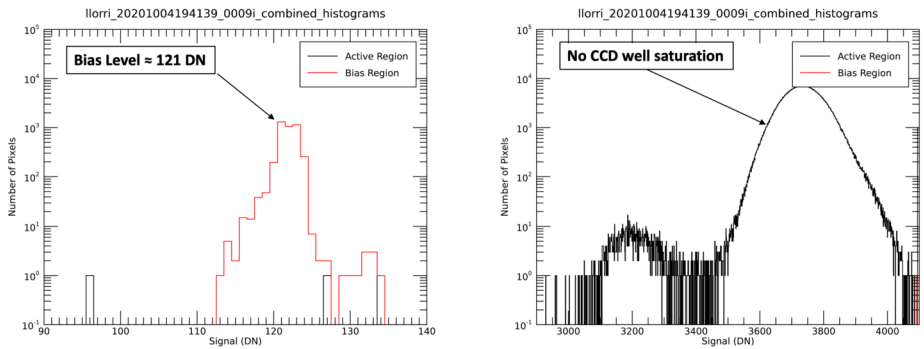


**Fig. 26** The plot on the left shows a histogram of the bias region of the CCD for the last non-saturated point in Fig. 25. The plot on the right shows the high end of the same histogram and shows no evidence of CCD charge well saturation out to at least a raw signal level of ~4000 DN. Since the bias level is ~121 DN, the net signal for linear response extends to at least ~3880 DN. Given that the electronics noise is ~0.9 DN, the dynamic range is ≥4310, which is ~44% larger than the requirement (3000)

### 4.2.6 Flats

Flat-fielding refers to the process of removing the pixel-to-pixel sensitivity variations in the image, which can be induced by either optical or CCD non-uniformity effects. An image obtained by illuminating the L’LORRI aperture uniformly with light is called a “flat.” During ground calibration testing, flats were obtained by using a calibrated integrating sphere to provide uniform illumination across the full L’LORRI aperture. Two different light sources were used, as described earlier, but they produced flats that differed by ≤1% for the vast majority of pixels. Flats were obtained in multiple thermal environments meant to mimic in-flight conditions, but they varied by ≤0.5% for the vast majority of pixels. Flats taken with the two different L’LORRI DPUs were essentially identical at the 0.1% level. The absolute intensity of the input illumination was measured using a calibrated photodiode.

The flat-field reference file used in the L’LORRI calibration pipeline was produced by averaging 100 flats taken when the OTA was at −85 C during the post-environmental calibration using weighted averages of flats from the two different light sources. These average images were debiased and desmeared, and then normalized to an average value of 1

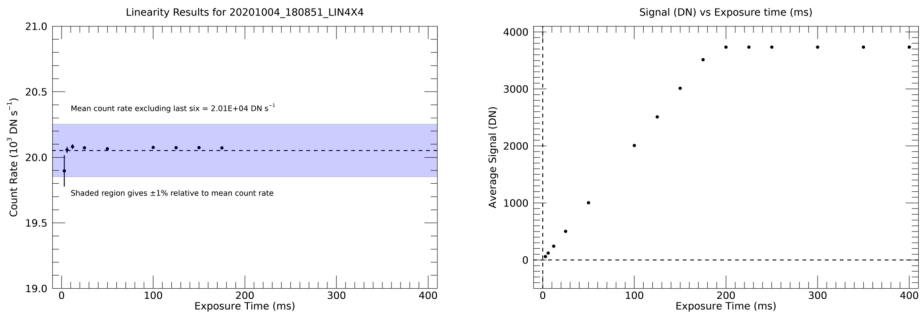


**Fig. 27** The plot on the left shows that the measured count rate for  $4 \times 4$  images is within 1% of the mean value for all exposure times (the blue shaded region), except for the saturated ones. The plot on the right shows that the response remains linear up to at least a net signal level of 3500 DN after bias subtraction

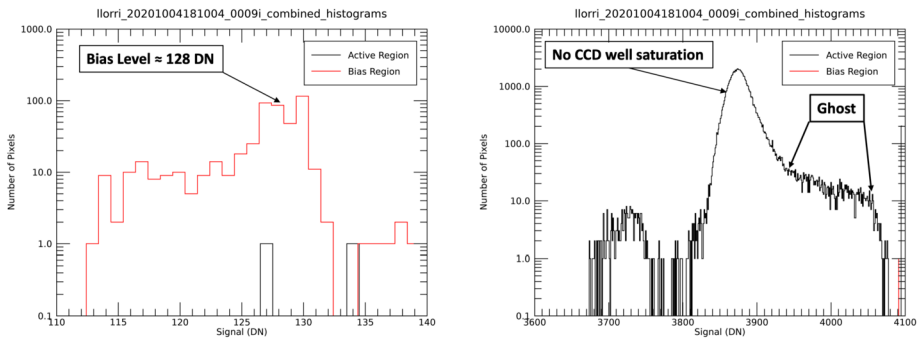


**Fig. 28** The plot on the left shows a histogram of the bias region of the CCD for the last non-saturated point in Fig. 27. The plot on the right shows the high end of the same histogram and shows no evidence of CCD charge well saturation out to at least a raw signal level of  $\sim 4060$  DN. Since the bias level is  $\sim 128$  DN, the net signal for linear response extends to at least  $\sim 3880$  DN. Given that the electronics noise is  $\sim 0.9$  DN, the dynamic range is  $\geq 4220$ , which is  $\sim 40\%$  larger than the requirement (3000)

(Fig. 29). The raw weighted average included a ghost of the field-flattening assembly near the center of the CCD (the integrating sphere overfilled the L’LORRI aperture) and scattered light near the bottom and right edges of the CCD. We tried to remove both of these artifacts, but their residuals are visible in the final flat, although only at the  $\sim 1\%$  level, or less.

If  $S$  (in units of DN) is an image of a target that has already been debiased and desmeared, and if  $FF$  is the reference flat-field image, then the flat-fielded (i.e., photometrically-corrected) target image ( $C$ ; units are DN) is given by  $C = S/FF$ . The effects of the CCD particles (Sect. 4.2.7) are almost completely removed by flat-fielding, except near the center of the most prominent particle located in the upper right of the CCD. That particle is approximately 17 pixels high by 7 pixels wide, and two of its pixels have normalized intensities of  $\sim 0.15$ , which means their effects are difficult to remove. Excluding row 0 and column 0, only 52 pixels in the L’LORRI flat have normalized intensities  $\leq 0.8$ , and 45 of those are in the single large particle. A histogram of the normalized flat is shown in Fig. 30.



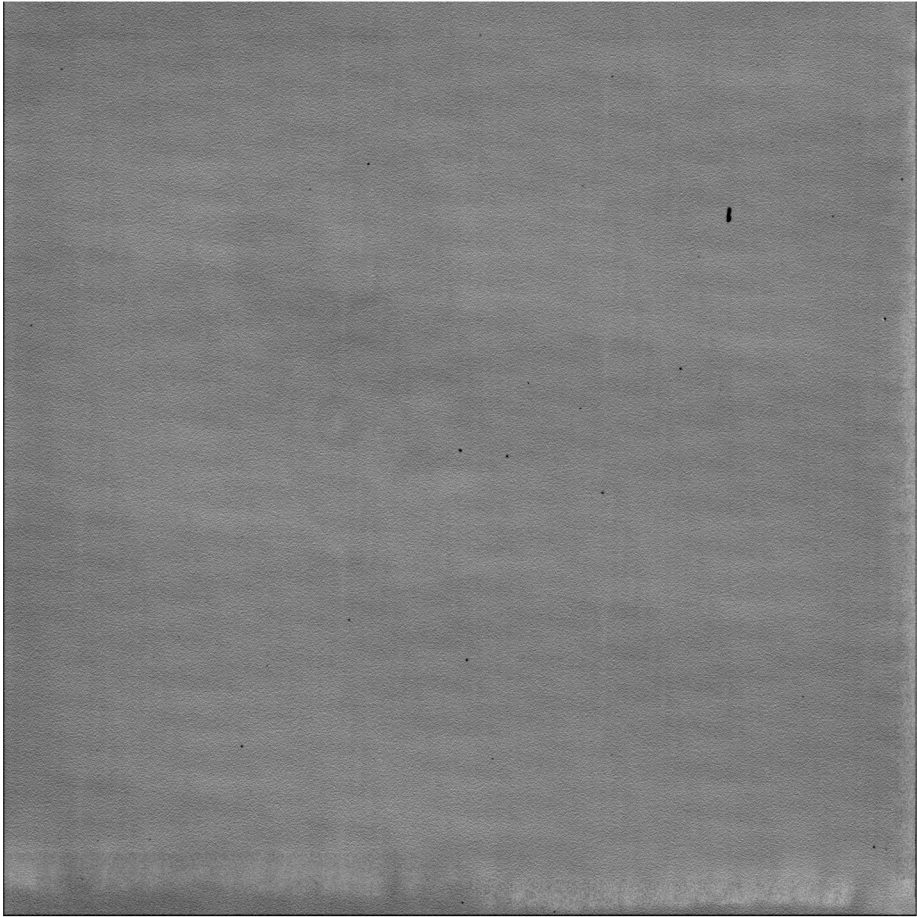


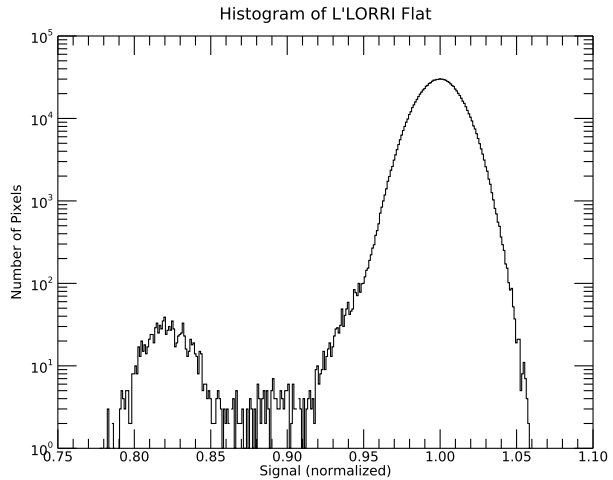
**Fig. 29** L'LORRI flat from a weighted average of 100 flats taken with two different lamps after subtraction of the central ghost and scattered light near the bottom and right edges. The image is displayed using a linear intensity scale ranging from 0.9 to 1.1. The prominent black area in the upper right is from a particle sitting on the CCD. Several smaller particles can also be seen across the image, but flat-fielding essentially removes all traces of them in the calibrated image. All the particles have been fixed in location on the CCD since September 2020

#### 4.2.7 Artifacts

As is the case with all instruments, L'LORRI has artifacts that must be considered when interpreting its images. Here we discuss two of L'LORRI's known artifacts: foreign object debris (FOD) on the CCD and L'LORRI's behavior when imaging bright sources that saturate the CCD full-well. Two other L'LORRI artifacts were discussed previously: optical ghosts were covered in Sect. 4.1.4, and the bias offset between the active and non-active regions of the CCD were covered in Sect. 4.2.1.

L'LORRI's CCD does not have a protective cover. Once the CCD is installed behind the OTA, dust and other particles (generally called FOD) can fall unimpeded onto the surface of the exposed CCD. Although we took great care to keep the area around the CCD clean, L'LORRI's environmental testing produced multiple opportunities for contamination events.

**Fig. 30** The figure shows a histogram of the L'ORRI normalized flat in Fig. 29. The vast majority of pixels lie within 10% of the histogram peak. The second histogram peak centered near 0.83 is comprised almost exclusively from pixels in row 1 of the CCD



During the instrument-level vibration testing at APL, when the OTA was mounted vertically with the CCD facing upwards, a rather large particle was shaken loose during the thrust-direction vibrate and fell down onto the CCD surface. This particle was displaced sideways by hundreds of CCD pixels during the subsequent vibrate in one perpendicular direction, but has since remained in its current location, including after another vibration perpendicular to the other two axes. The particle also did not move during the spacecraft-level vibration during ATLO. Perhaps this particle was displaced from the L'ORRI lens assembly; we had previously noticed FOD within the lens assembly but could not remove it after the OTA was assembled. In any case, this large particle has now been in the same location for over a year, which suggests it is now a permanent feature.

Figure 31 shows a magnified view of the L'ORRI flat field centered on the large FOD. The particle has dimensions of approximately 17 pixels (0.221 mm) by 7 pixels (0.091 mm) with 45 pixels having transmittances  $\leq 0.80$ . Two of the pixels have transmittances of  $\sim 0.15$  and are not removed by the flat-fielding process used to produce calibrated L'ORRI images. Thus, we have marked these two pixels as “bad” in the quality factor extension of the calibrated FITS image. There is other FOD on the CCD (see Fig. 29), but their effects are minimal because the flat-fielding process essentially removes them in the calibrated image.

Saturated images of point sources can also produce artifacts in L'ORRI images. These were characterized most extensively for the EM FPU on 2020 May 29 under ambient laboratory conditions in the APL cleanroom during illumination of the OTA by a LUPI using red laser light. Point source saturation effects for L'ORRI were also measured during the pre-environmental calibration test with the FM FPU, but the degree of saturation was much less than explored during the earlier testing. No point source saturation tests were conducted during the post-environmental calibration.

The *New Horizons* LORRI images of bright stars in  $4 \times 4$  format have “black tails” (when the image is displayed using a grayscale ranging from black for the lowest DN values and white for the high DN values) along the CCD row direction, which is due to amplifier undershoot/overshoot in response to a rapidly changing analog input signal. This effect has essentially been eliminated in L'ORRI images, but another artifact has been introduced for high levels of saturation. As shown in Fig. 32 and Fig. 33, the bias level in the rows above the row containing the saturated target is depressed by up to  $\sim 30$  DN when the input light is  $\sim 100$  times the saturation level. This produces a dark area in the image that spans entire

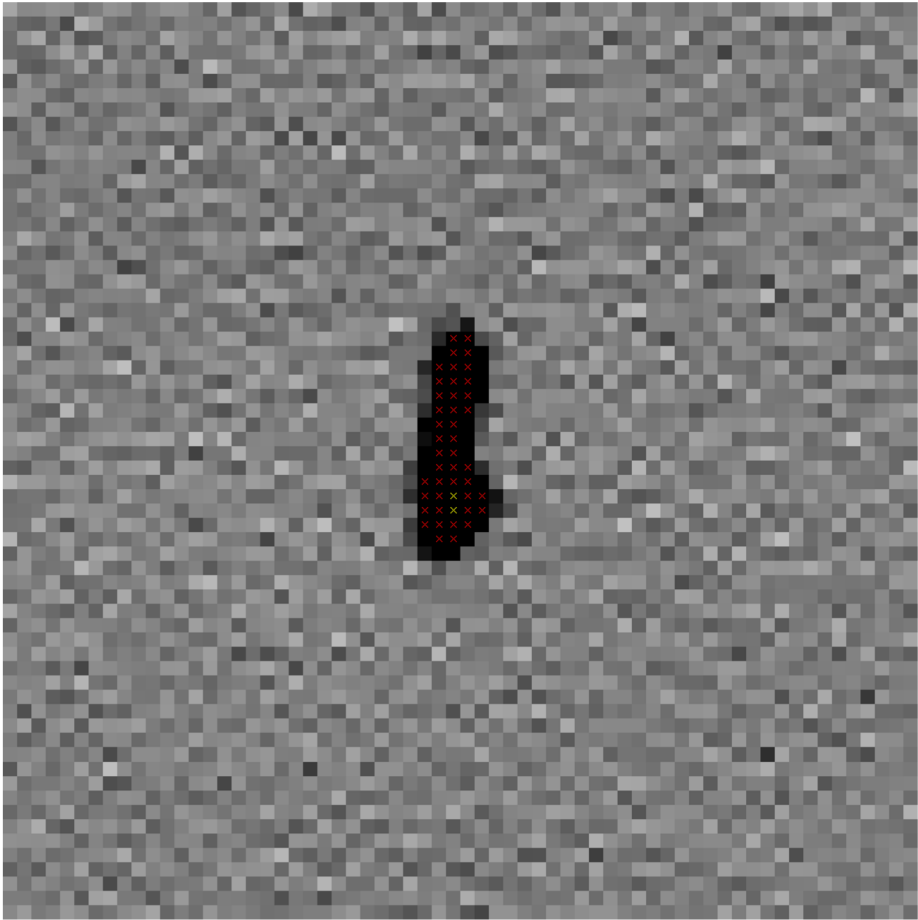


**Fig. 31** Magnified view ( $64 \times 64$  pixels) of the L'LORRI flat field image (see Fig. 29) centered on the largest particle (also called “foreign object debris,” or FOD) lying on the CCD. Red X symbols mark where the normalized transmittance is  $\leq 0.80$ ; the two pixels where the transmittance is  $\sim 0.15$  are marked with yellow X symbols. This particle is approximately 17 pixels (0.221 mm) by 7 pixels (0.091 mm), and there are a total of 45 pixels with transmittances  $\leq 0.80$

CCD rows (Fig. 32). Row profiles in the region of the saturated pixel also show different bias levels on either side of the saturated pixels (i.e., left-to-right asymmetry; see Fig. 33).

When individual pixels are saturated in  $4 \times 4$  format, very high amplitude analog signals are presented to the ADC possibly causing its internal protection diodes to activate and start discharging the reference capacitors. Recovery back to the nominal bias level is estimated to take  $\sim 6$  ms (based on the relevant circuit's RC time constants), which corresponds to  $\sim 8$  rows worth of pixel readout time, which roughly corresponds to the size of the “dark rows” artifact. No similar effect has ever been observed in *New Horizons* LORRI images, nor has been it observed in L'LORRI  $1 \times 1$  images. Since all the close flyby imaging of *Lucy's* targets will be taken in  $1 \times 1$  format, we do not expect this dark rows artifact to be an issue for the L'LORRI images taken near the time of closest approach. Perhaps, however, this artifact

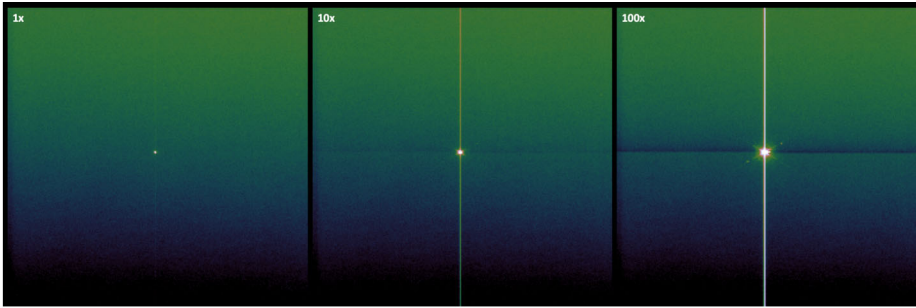


**Fig. 32** Three different raw  $4 \times 4$  L'LORRI images with different levels of pixel saturation are shown: 1, 10, and 100 times saturated from left to right. The number of saturated pixels in the images are 1, 5, and 13 respectively. The exposure time was 50 ms in each case, and the light intensity was increased by using different levels of neutral density filters. All images are displayed using an ASINH intensity stretch ranging from 290 DN to 4095 DN and a “cubehelix” color scale for better visibility of different intensity levels. The vertical streak is associated with the CCD frame transfer (*not* CCD charge bleeding) and becomes stronger as the input light becomes brighter. As the input light level becomes stronger, a dark region extending across entire CCD rows becomes more prominent. All the images were taken in a cleanroom under ambient laboratory conditions and have an intensity ramp from the bottom to the top of the CCD owing to dark current accumulated during the readout from bottom to top (there is more time to integrate dark signal for the pixels in the higher rows). See the text for further discussion

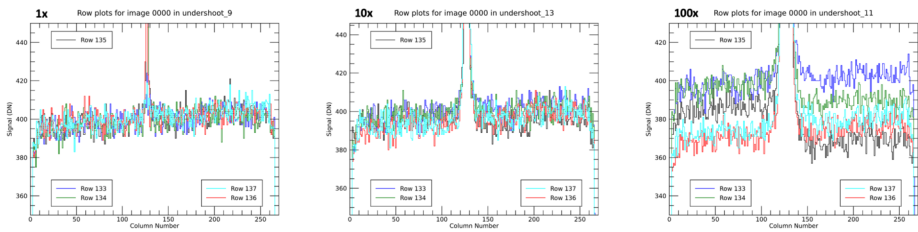


**Fig. 33** Row profiles across the images in Fig. 32 are displayed. In each plot, the intensity profile for the row containing the pixel with the brightest light, as well as profiles for  $\pm 2$  rows about that peak row, are displayed. For the image with one saturated pixel ( $1 \times$  saturation), all the row profiles lie on top of each other. For the  $10 \times$  saturated image, there is an offset of  $\sim 5$  DN between the right hand and left hand sides (i.e., relative to the peak column) of the peak row (row 135), but there are no offsets for the other rows. For the  $100 \times$  saturated image, there is a left-right offset of  $\sim 5$  DN for one row below the peak row (row 134), and the lower rows have systematically larger signal than the upper rows

might be seen if there are bright stars in the background field during deep observations taken to search for potential satellites near *Lucy* targets.

### 4.3 System Throughput

For sensitivity considerations, we consider two types of targets: “point” and “diffuse”. A point source is one that is not spatially resolved by L'LORRI (e.g., “star-like”), as will be the case for distant observations of the *Lucy* mission targets (e.g., for initial OpNav target acquisition) and searches for unresolved satellites. A “diffuse” source is one that is spatially resolved by L'LORRI, as will be the case during near-encounter observations of the surfaces of the *Lucy* mission targets.

For a photon counting optical system like L'LORRI, the signal detected ( $S$  in electrons) in an image pixel with exposure time  $t$  (in seconds) can be expressed as:

$$S = t \Omega \int_{\lambda} I A_{\text{eff}} d\lambda = t \Omega A \int_{\lambda} I \text{QE} d\lambda \quad (\text{diffuse target}) \quad (1)$$

$$S = t \text{EE} \int_{\lambda} F A_{\text{eff}} d\lambda = t \text{EE} A \int_{\lambda} F \text{QE} d\lambda \quad (\text{point target}) \quad (2)$$

And the noise ("N" in electrons) can be expressed as (for both diffuse and point targets):

$$N = \sqrt{S + SL + FT + (I_d t) + RN^2} \quad (3)$$

Where:

$\Omega$  = pixel IFOV (sr)

$A$  = unobscured input aperture area (cm<sup>2</sup>) of the OTA

$A_{\text{eff}}$  = System effective area =  $A * \text{QE}$  (cm<sup>2</sup>)

$\text{QE}$  = system quantum efficiency (dimensionless; including all losses)

$\text{EE}$  = ensquared energy = fraction of point source total signal contained in peak pixel (dimensionless)

$I$  = diffuse target's radiance (photons cm<sup>-2</sup> s<sup>-1</sup> sr<sup>-1</sup> nm<sup>-1</sup>)

$F$  = point target's flux, or irradiance (photons cm<sup>-2</sup> s<sup>-1</sup> nm<sup>-1</sup>)

$SL$  = signal produced by solar scattered light (electrons)

$FT$  = signal produced by the CCD frame transfer process (electrons)

$I_d$  = CCD dark current (electrons s<sup>-1</sup> pixel<sup>-1</sup>)

$RN$  = electronics noise (electrons; includes the CCD read noise)

The integrals are over all wavelengths.

The L'LORRI signal level depends on two key parameters: the total system quantum efficiency (QE) and (in the point source case) the amount of energy from a point source concentrated in a single pixel (EE). We already discussed EE in Sect. 4.1.2. For point sources with  $\text{SNR} \geq 5$  in a single pixel, the SNR can typically be improved by a factor of  $\sim 2$  by summing the signal over several pixels (aperture photometry) or by employing PSF fitting photometry. These techniques can be employed when the SNR is only marginally above the requirement for a single pixel.

The system quantum efficiency (QE) is given by:

$$\begin{aligned} \text{QE} &= A_{\text{eff}}/A = L_{\text{obscure}} T_{M1} T_{M2} T_{L1} T_{L2} T_{L3} \text{QE}_{\text{CCD}} \\ &= L_{\text{obscure}} T_{\text{optics}} \text{QE}_{\text{CCD}} \end{aligned} \quad (4)$$

Where:

$L_{\text{obscure}}$  = loss factor associated with obscuration by the secondary mirror and OTA spider

$T_x$  = transmittance of the individual optical element "X"

$M1$  = OTA primary mirror

$M2$  = OTA secondary mirror

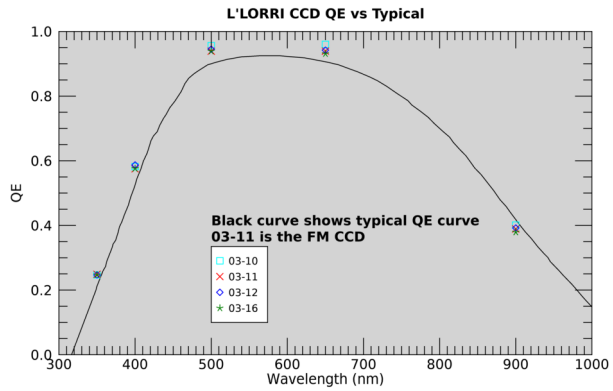
$L1$  = first lens in the field flattener lens assembly

$L2$  = second lens in the field flatter lens assembly

$L3$  = third lens in the field flatter lens assembly

$T_{\text{optics}}$  = total transmittance of all optical elements

**Fig. 34**  $QE_{CCD}$  curves were measured by Teledyne-e2v for each of the devices procured for L'LORRI. In all cases, the L'LORRI values lie above the “typical” QE curve over most of the optical wavelength range. Device 03-11 was selected as the L'LORRI flight CCD



$QE_{CCD}$  = Quantum Efficiency of the CCD

Note that  $A = \pi(20.8)^2/4 = 339.8 \text{ cm}^2$  (a L'LORRI requirement is that the M1 mirror must have a clear aperture  $\geq 20.8 \text{ cm}$ ) and  $L_{\text{obscure}} \geq 0.88$  (another L'LORRI requirement).

Although not explicitly stated in the equation above, all quantities in the QE equation are a function of wavelength, except  $A$  and  $L_{\text{obscure}}$ . L'LORRI is a panchromatic instrument, which means that its output signal is proportional to the integral of the above factors over all wavelengths.

We refer to the “pivot” wavelength ( $\lambda_{\text{pivot}}$ ), which is one way of characterizing the “effective” wavelength for a broadband optical instrument. The pivot wavelength is defined as:

$$\lambda_{\text{pivot}} = \sqrt{\frac{\int QE * \lambda \, d\lambda}{\int QE/\lambda \, d\lambda}} \tag{5}$$

The pivot wavelength for L'LORRI is calculated to be 603.0 nm, whereas *New Horizons* LORRI had a pivot wavelength of 607.6 nm.

L'LORRI is designed to have the same QE as LORRI, or better. In setting the transmittance requirements for the optical elements, APL specified to L3H that the transmittances for the L'LORRI optical elements must be greater than, or equal to, the measured LORRI values. L3H used the same optical coating prescriptions for the M1 and M2 mirrors that LORRI used, but the original coating vendor is no longer in business. Nevertheless, the new optical coating vendor (Infinite Optics Incorporated, IOI) achieved transmittances consistent with the L'LORRI specifications. As previously noted, the spare LORRI M1, after precision cleaning at L3H, became the flight M1 for L'LORRI. The transmittance data from IOI for the L'LORRI lens assembly was essentially identical (to within 2%) to the LORRI values.

L'LORRI uses the same model CCD (CCD47-20), with the same specifications (backside-thinned, backside-illuminated, with “Midband AR” coating and anti-blooming) and the same vendor (formerly e2v, now Teledyne-e2v), as used on LORRI. The CCD quantum efficiency ( $QE_{CCD}$ ) is determined by the AR coating and the intrinsic response of the silicon substrate. The vendor provided  $QE_{CCD}$  measurements for each CCD delivered to the L'LORRI program, and the curves lie above the “typical” values for all the CCDs (Fig. 34).

Figure 35 shows the LORRI system QE as a function of wavelength, as determined from the absolute calibration measurements of the solar-type reference star HD 37962. The LORRI system QE is approximately 50% over much of the visible wavelength range (e.g., 480–700 nm). LORRI is a panchromatic instrument, which means that its output signal is

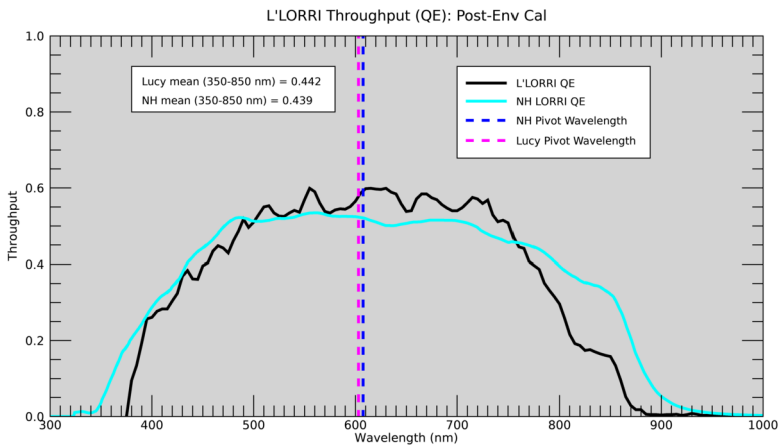


**Fig. 35** The system quantum efficiency (QE) is plotted as a function of wavelength for both L'LORRI and LORRI. The mean QE over the wavelength range 350–850 nm is  $\sim 44\%$  for both L'LORRI and LORRI. The locations of the L'LORRI and LORRI pivot wavelengths are shown, as are the standard visible photometric bands in the Johnson-Landolt system. L'LORRI's pivot wavelength is located between the standard *V* and *R* band wavelengths

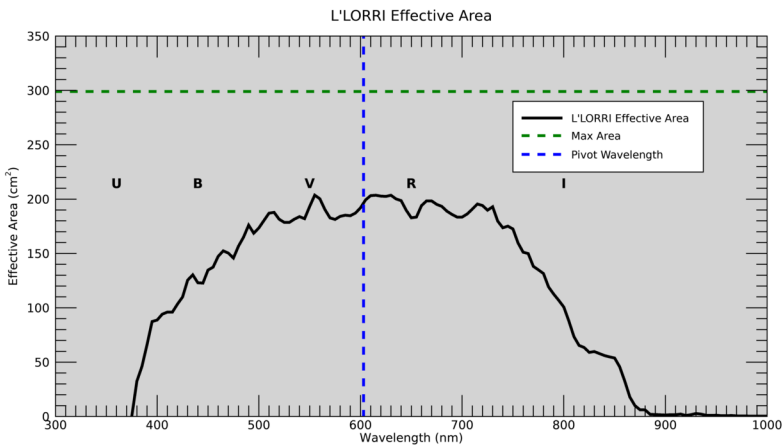


**Fig. 36** LORRI's effective area is plotted as a function of wavelength. Given the estimated L'LORRI obscuration of  $\sim 12\%$ , the theoretical maximum effective area is given by the green dashed line. The locations of the L'LORRI pivot wavelength and the standard visible photometric bands are also shown

proportional to the integral over all wavelengths of the product of the QE and the target's SED.

The commonly used quantity “effective area” ( $A_{\text{eff}}$ ) of the optical system is just the area of L'LORRI's input aperture ( $A = \pi * 20.8^2 / 4 = 339.8 \text{ cm}^2$ ) multiplied by the system QE. Given the estimated L'LORRI obscuration of  $\sim 12\%$  (i.e.,  $L_{\text{obscure}} = 0.88$ ), the largest possible effective area for L'LORRI is  $\sim 300 \text{ cm}^2$ . Figure 36 shows the L'LORRI effective area as a function of wavelength.

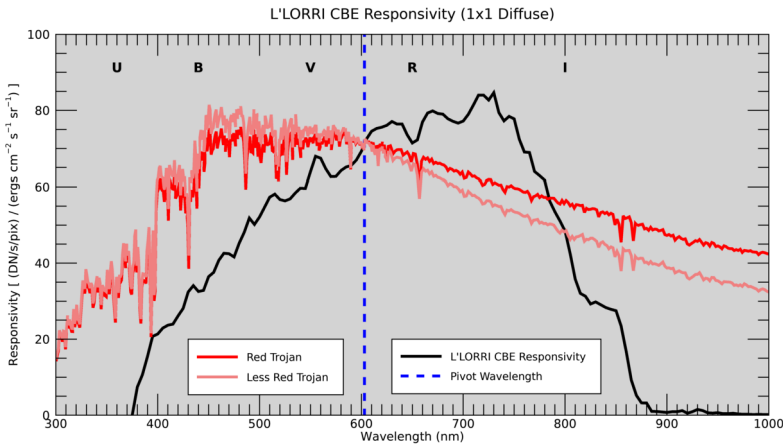


**Fig. 37** L'ORRI's absolute responsivity is plotted as a function of wavelength. The in-flight measurements of an absolute calibration standard star indicate that these values should be multiplied by 1.139. Normalized spectra of the two types of Trojan spectra ("Red" and "Less Red") are overlain for comparison. The locations of the L'ORRI pivot wavelength and the standard visible photometric bands are also shown

The L'ORRI absolute responsivity curve, which enables the conversion from engineering units to physical units, can be derived from the QE curve using the following equation:

$$R_{\lambda} = A_{\text{eff}} * \Omega * \lambda / \text{gain} / hc \tag{6}$$

where:

- $R_{\lambda}$  is the responsivity ( $[\text{DN s}^{-1} \text{ pixel}^{-1}] / [\text{ergs cm}^{-2} \text{ s}^{-1} \text{ sr}^{-1}]$ )
- $A_{\text{eff}}$  is the effective area as defined above ( $\text{cm}^2$ )
- $\Omega$  is the solid angle of a single pixel (sr)
- $\lambda$  is the wavelength of interest ( $\text{\AA}$ )
- gain is the CCD gain ( $\text{e DN}^{-1}$ )
- hc is the product of Planck's constant and the speed of light ( $1.986 \times 10^{-8} \text{ ergs-\AA}$ )

Figure 37 shows the L'ORRI responsivity curve for  $1 \times 1$  format based on results from the ground calibration program. The responsivity curve for  $4 \times 4$  format can be obtained by multiplying the  $1 \times 1$  curve by 16.4. The figure also compares the L'ORRI responsivity curve to the spectral energy distributions (SEDs) of the two types of Trojans being targeted by the *Lucy* mission ("Red" and "Less Red", or "Gray"). The L'ORRI response to the Trojans is the integral of the product of the Trojan's SED and the L'ORRI responsivity.

We used the ground calibration mainly to characterize the *relative* sensitivity as a function of wavelength. The absolute sensitivity based on the ground calibration was expected to be accurate to  $\sim 10\text{-}20\%$ . Our best estimate for L'ORRI's absolute sensitivity will be derived from data taken during in-flight observations of an absolute calibration standard star. The irradiance (or flux) of the calibration stars we plan to use for L'ORRI are known to an absolute accuracy of  $\sim 1\%$  from observations made by the *Hubble Space Telescope*. As discussed later, the first in-flight observation of an absolute calibration standard showed that L'ORRI's absolute response is  $\sim 14\%$  larger than the nominal value from the ground calibration.

For a target whose spectral energy distribution (SED) is similar to that of the standard star, the L'ORRI absolute calibration should be accurate to a similar accuracy. However,



for *Lucy* targets with SEDs significantly different from the SED of the calibration star, we estimate that the L’LORRI absolute calibration in those cases should be accurate to ~10–20% (i.e., similar to the accuracy of the ground calibration).

A L’LORRI exposure time calculator (ETC), which uses the responsivity curve discussed above, already exists. The ETC has recently been updated to include the results from the in-flight observation of an absolute calibration standard star. This ETC is used for both planning future observations (e.g., estimating SNR for planned observations) and for analyzing completed observations (e.g., for converting L’LORRI signals from engineering units into absolutely calibrated scientific units). The ETC includes noise from: the electronics, shot noise from the target itself, shot noise associated with CCD frame transfer process (i.e., frame transfer smear), shot noise from the CCD dark current (generally negligible), and shot noise from solar scattered light when the solar elongation angle (SEA) is  $\leq 90^\circ$ . The ETC also permits selection of the fraction of the total signal from a point source that falls within the peak pixel (i.e., EE).

The L’LORRI calibration pipeline provides photometrically corrected images, but the intensities are still in engineering units (DN). Pixel intensities can be converted to scientific units using photometry keywords provided in the image data file. In Table 6, we provide photometry keywords for objects with three different SEDs: solar-like, similar to the average “red” Trojan spectrum, and similar to the average “gray” Trojan spectrum. We provide here two examples showing how to convert from engineering units to physical units: one for a diffuse target and one for a point (i.e., unresolved) target.

Consider a diffuse target whose spectrum is similar to that of red Trojan globally averaged SED. In this case, the RTROJANR photometry keyword in the header of the calibrated image should be used to convert from the observed count rate in a pixel to a radiance value at L’LORRI’s pivot wavelength:

$$I = S/t_{\text{exp}}/\text{RTROJANR (diffuse target)} \tag{7}$$

where:

*I* is the diffuse target radiance (ergs cm<sup>-2</sup> s<sup>-1</sup> Å<sup>-1</sup> sr<sup>-1</sup>) at  $\lambda_{\text{pivot}}$

*S* is the measured signal in a pixel (DN)

*t<sub>exp</sub>* is the exposure time (s)

RTROJANR is the L’LORRI diffuse photometry keyword for targets with an SED similar to a red Trojan

Since the solar flux (*F<sub>☉</sub>*) at a heliocentric distance of 1 AU at the L’LORRI pivot wavelength is 176 ergs cm<sup>-2</sup> s<sup>-1</sup> Å<sup>-1</sup>, the value for the radiance can be converted to *I/F* (where  $\pi F = F_{\odot}$ ), which is a standard photometric quantity used in planetary science, using:

$$I/F = \pi I r^2 / F_{\odot} \tag{8}$$

$$\rightarrow I/F = (S/t_{\text{exp}}/\text{RTROJANR}) * \pi r^2 / F_{\odot} \tag{9}$$

where “*r*” is the target’s heliocentric distance in au.

For unresolved targets (e.g., planetary targets observed at large ranges), the absolutely calibrated flux (also called the “irradiance”) at the L’LORRI pivot wavelength can be determined using the point source photometry keywords. For a target with an SED similar to that of gray Trojan, the observed count rate integrated over the LORRI PSF can be related to the flux (not to be confused with “*F*” in “*I/F*”) at the L’LORRI pivot wavelength by:

$$F = S_{\text{total}}/t_{\text{exp}}/\text{PTROJANG (point target)} \tag{10}$$

**Table 6** L'LORRI photometry keywords

Keyword	Value ( $1 \times 1$ )	Value ( $4 \times 4$ )
RSOLAR	$2.713 \times 10^5$	$4.455 \times 10^6$
RTROJANR	$2.784 \times 10^5$	$4.571 \times 10^6$
RTROJANG	$2.712 \times 10^5$	$4.453 \times 10^6$
PSOLAR	$1.101 \times 10^{16}$	$1.130 \times 10^{16}$
PTROJANR	$1.130 \times 10^{16}$	$1.160 \times 10^{16}$
PTROJANG	$1.101 \times 10^{16}$	$1.130 \times 10^{16}$

The keywords starting with “R” are diffuse target sensitivity keywords and their values have units of  $(\text{DN s}^{-1} \text{ pixel}^{-1}) / (\text{ergs cm}^{-2} \text{ s}^{-1} \text{ \AA}^{-1} \text{ sr}^{-1})$ . The keywords starting with “P” are point target sensitivity keywords and their values have units of  $(\text{DN s}^{-1}) / (\text{ergs cm}^{-2} \text{ s}^{-1} \text{ \AA}^{-1})$ . For point targets, the signal refers to values integrated over the entire instrumental PSF.

where:

$F$  is the point target flux, or irradiance ( $\text{ergs cm}^{-2} \text{ s}^{-1} \text{ \AA}^{-1}$ )

$S_{\text{total}}$  is the total signal from the target integrated over the PSF (DN)

$t_{\text{exp}}$  is the exposure time (s)

PTROJANG is the L'LORRI point source photometry keyword for targets with an SED similar to a gray Trojan

When observing stars, it is more common to convert the absolute flux to a magnitude in a standard photometric system. For convenience to users, we provide a prescription for converting L'LORRI signal rates to standard  $V$  magnitudes in the Johnson photometric system:

$$V = -2.5 \log(S/t_{\text{exp}}) + \text{ZPT} + \text{CC} - \text{AC} \quad (11)$$

where  $V$  is the magnitude in the standard Johnson  $V$  band (i.e., specifies the target's flux at  $5500 \text{ \AA}$ ),  $S$  (DN) is the measured signal in the selected photometric aperture,  $t_{\text{exp}}$  (s) is the exposure time, ZPT is the photometric zero point (18.93 for  $1 \times 1$  and 18.96 for  $4 \times 4$ ), CC is a color correction term (as specified in Table 7), and AC is an aperture correction term to convert from the flux collected in a specified synthetic aperture to the total flux integrated over the L'LORRI PSF.

The CC terms listed in Table 7 were calculated using SEDs for the listed blackbody temperatures, which roughly correspond to the listed stellar spectral types. We used the two generic types of Trojan spectra (“red” and “gray”), as adopted by the *Lucy* mission science team, to estimate CC for those cases. For typical L'LORRI observations of point sources, the SNR is optimized by integrating over a circular aperture with a radius of 5 pixels ( $1 \times 1$  format) or 3 pixels ( $4 \times 4$  format), in which case AC is either 0.10 or 0.00, respectively.

For example, the  $V$  magnitude for an A-type star observed by L'LORRI is given by:

$$V_{\text{star}} = -2.5 \log(S_{\text{total}}/t_{\text{exp}}) + \text{ZPT} - 0.036 \quad (12)$$

where  $V_{\text{star}}$  is the star's magnitude in the standard Johnson  $V$  band,  $S_{\text{total}}$  is the total signal integrated over the L'LORRI PSF (DN),  $t_{\text{exp}}$  is the exposure time (s), ZPT is the photometric zero point (18.93 for  $1 \times 1$  and 18.96 for  $4 \times 4$ ), and the color correction term is  $-0.036$ .

**Table 7** Approximate L'LORRI color corrections

$T_{bb}$	Spectral Type	Color Correction (CC)
30,000	O ( $\geq 30,000$ )	-0.071
10,000	B (10,000–30,000)	-0.071
7500	A (7500–10,000)	-0.036
6000	F (6000–7500)	+0.027
5200	G (5200–6000)	+0.093
5800	G2V (5800)	+0.040
–	Sun	+0.00
3700	K (3700–5200)	+0.39
2400	M (2400–3700)	+1.2
–	Red Trojan	+0.028
–	Gray Trojan	-0.00

$T_{bb}$  is the blackbody temperature that describes the spectral energy distribution (SED) used to calculate the L'LORRI signal rate for a target assuming the same  $V$  magnitude for all listed temperatures. The Spectral Type refers to the stellar classification assigned to a star whose effective temperature is in the range listed in parentheses, with the starting value equal to  $T_{bb}$ , except we used the actual SED of the Sun for that case. The Color Correction (CC) is the value that must be added to the raw  $V$  to correct for the SED of the target (see equation (11)). We used the two generic types of Trojan spectra (“red” and “gray”), as adopted by the *Lucy* mission science team, to estimate CC for those cases. Since target SEDs are rarely matched exactly by a blackbody SED, CC only provides an approximate color correction for converting L'LORRI count rates ( $\text{DN s}^{-1}$ ) to Johnson  $V$  magnitude. If the SED of the target is known, the L'LORRI ETC can be used to produce a more accurate CC value.

#### 4.4 Optical Navigation and Satellite Searches

L'LORRI is the *Lucy* mission's primary optical navigation camera. For each encounter, L'LORRI imaging will begin two months in advance of each flyby. Subsequent systematic observations by L'LORRI will be used by the optical navigation team to determine the trajectory correction maneuvers (TCMs) needed to guide the *Lucy* spacecraft to its designed aim point relative to each target.

All of *Lucy*'s targets should be detectable by L'LORRI two months in advance of closest approach in co-added  $1 \times 1$  images, but a few of the targets are near the sensitivity limit. In those cases, it will be prudent to take  $4 \times 4$  images as well to guarantee detection of the target.

The search for potential satellites near each *Lucy* target is another important L'LORRI objective. By co-adding multiple  $4 \times 4$  images, L'LORRI should be able to detect any satellites larger than  $\sim 2$  km in diameter in the orbital stability zone of each *Lucy* target. Further discussion of the *Lucy* satellite search program can be found elsewhere in this collection (Noll et al. 2023).

### 5 Initial in-Flight Results

After the launch of the *Lucy* spacecraft in October 2021, L'LORRI was used during a variety of activities in the following year (Table 8). The initial commissioning was conducted  $\sim 1$  month after launch to verify L'LORRI's basic functionality. These tests were conducted while the L'LORRI hardware was at relatively high temperatures to enhance outgassing but

**Table 8** Main L'LORRI inflight activities during the first year after launch

Dates (UTC)	Activity	Comments
2021 Nov 08	Initial commissioning	Nominal engineering performance, all operating modes verified, data transfers verified
2022 Feb 14	IPP calibration	Success, nominal instrument alignments
	Pointing stability	Nominal performance verified
	Limited straylight test	Nominal performance verified
	Throughput measurement	Nominal performance verified
	PSF with OTA at $-85^{\circ}\text{C}$	Slightly degraded relative to nominal prediction, but still meets requirement over most of the FOV
2022 May 15,16	Earth-Moon solar eclipse observations	Successful observations
	Full Functional Test	Nominal performance verified
	PSF with OTA at $-95^{\circ}\text{C}$	Successful, but very limited data
2022 Sep 26,27	DART impact observations	Successful campaign conducted
2022 Oct 16	Scattered light/Ghost test	Nominal performance verified
	Lunar crater imaging	PSF limits accuracy of crater counts
	PSF with OTA at $-95^{\circ}\text{C}$	Data suggest modest improvement relative to $-85^{\circ}\text{C}$ , but more data needed
	Trigger mode test	Successful demo during lunar scan
	L' TES co-alignment check	Success

“Nominal performance” means the data lie within the predicted range. See the text for further discussion.

were still suitable for checking voltages, currents, and a suite of instrument functions. All L'LORRI engineering data and instrument functions were nominal during this testing. We verified that every L'LORRI operational mode worked as designed, the internal calibration lamps operated as expected, and all data were transferred properly from L'LORRI to the spacecraft and then from the spacecraft to the ground. The optical performance could not be checked at this time because the high OTA temperature (near  $0^{\circ}\text{C}$ ) meant that the telescope was badly out of focus, but stars could be seen and were used to verify that the spacecraft pointing accuracy was within its specified requirements.

The first opportunity to check L'LORRI's optical performance when the OTA was near its originally planned operating temperature ( $-85^{\circ}\text{C}$ ) was in February 2022. The primary objective of those observations was to measure the relative boresight locations of L'LORRI, TTCam, and Ralph-MVIC and calibrate the instrument pointing platform (IPP) by pointing at multiple different locations using IPP motions; all of these tasks were performed successfully and the measurements indicated nominal performance.

The February 2022 plan was loaded with several other activities designed to characterize L'LORRI's performance. One set of images was taken at a solar elongation angle of  $85^{\circ}$ , and the solar scattered light level was only  $\sim 60\text{-}65\%$  of the value of the predicted value based on NH-LORRI data. We took images of the extremely bright star Bellatrix ( $V = 1.64$ ) to characterize optical ghosts (nominal performance), the far-field PSF (achieved), and our ability to accurately remove frame transfer smear for the shortest exposure time of 1 ms (achieved). We obtained a series of images of the solar-type (G2V) absolute calibration star HD 37962, using both CCD formats and both DPUs, to measure the total system throughput (Fig. 38).

**Table 9** Adopted magnitudes and fluxes

Object	$B$	$V$	$R$	$F_B$	$F_V$	$F_R$
Star-0	0.000	0.000	0.000	$6.96 \times 10^{-09}$	$3.66 \times 10^{-09}$	$2.18 \times 10^{-09}$
Sun	-26.055	-26.771	-27.158	$1.84 \times 10^{+02}$	$1.87 \times 10^{+02}$	$1.59 \times 10^{+02}$
HD 37962	8.528	7.810	7.446	$2.70 \times 10^{-12}$	$2.75 \times 10^{-12}$	$2.29 \times 10^{-12}$

“Star-0” refers to an unresolved target whose spectral energy distribution (SED) gives 0 mag in the Johnson-Kron-Cousins ( $BVR$ ) stellar magnitude system. The adopted central wavelengths of the  $B$ ,  $V$ , and  $R$  bands are 4400 Å, 5500 Å, and 6500 Å, respectively. The listed fluxes ( $F_B, F_V, F_R$ ) are in  $\text{ergs cm}^{-2} \text{s}^{-1} \text{Å}^{-1}$  and are mean values in  $\pm 50$  Å regions centered on these wavelengths. The values for the Sun and HD 37962 are derived from spectroscopic data archived in a calibration database maintained by the Space Telescope Science Institute (STScI). The Star-0 fluxes are calculated using spectral data of the calibration star Vega ( $\alpha$ -Lyrae), assuming Vega has  $V = 0.035$  in all wavelength bands. See the text for further discussion.

The analysis of these latter observations deserves more discussion owing to some subtle issues regarding the absolute calibration. We had previously assumed (Weaver et al. 2020) that HD 37962 had  $V = 7.850$  and  $B - V = 0.65$ , but we recently noticed discrepancies with values reported from other sources. For example, DR10 (data release 10) from the AAVSO Photometric All-Sky Survey (APASS) assigns the following magnitudes to HD 37962:  $V = 7.881$  (no error is given and is presumed to be near 0),  $B = 8.662 \pm 0.039$ , which are both fainter and redder ( $B - V = 0.781 \pm 0.039$ ) than what we have been using. Gaia measurements and photometric relations found in Evans et al. (2018) can be used to derive  $V = 7.829$  for HD 37962. Given these discrepancies, we decided to establish our own magnitude values for HD 37962 using the irradiance (or flux) measured by the *Hubble Space Telescope*, which has an absolute accuracy of  $\sim 1\%$ . The results are given in Table 9. L'LORRI's absolute sensitivity is  $\sim 14\%$  larger than the value determined from the ground calibration and  $\sim 19\%$  larger than the value measured for LORRI.

An extensive set of observations were performed near the star S Monocerotis ( $V = 4.5$ ) in the open star cluster NGC 2264 to study the effects of spacecraft jitter and exposure time on the quality of the PSF (Fig. 39). The spacecraft pointing moves around at the level of  $\sim 1''$  even during inertial pointings, but that generally doesn't affect the PSF quality except possibly for exposure times longer than about 30 s (the longest available exposure time is 64.9 s).

The images of stars taken during the February 2022 observations were slightly more elongated than expected (Fig. 40). Although we knew from ground testing that the L'LORRI OTA had significant astigmatism and would be significantly out-of-focus when operated at cold temperatures (see the earlier discussion), we were expecting the in-flight PSF to be somewhat *better* than the ground PSFs owing to the various issues (mainly uncontrolled vibrations) that artificially broadened the PSFs measured during the ground calibration.

Figure 41 compares the FWHMs across the FOV for one of the ground tests versus the in-flight case, both taken with the OTA primary mirror near  $-85$  C. Although the spatial pattern of the PSFs is different for the two cases (for reasons we don't yet understand), the FWHMs for the in-flight case tend to be slightly larger (by  $\sim 0.1$  pixel) than the values for the ground case. The requirement that the PSF must have  $\text{FWHM} \leq 3$  pixels is satisfied for both cases across most of the FOV, but the region where the requirement is met is slightly larger for the ground case. The temperature gradient across the OTA (represented by the M1–M2 temperature difference) appears to be slightly larger for the in-flight case (1.1 C for ground versus 2.7 C for in-flight), which might partially explain its slightly poorer performance, but we have no data to verify that. In any case, we were motivated by these initial in-flight

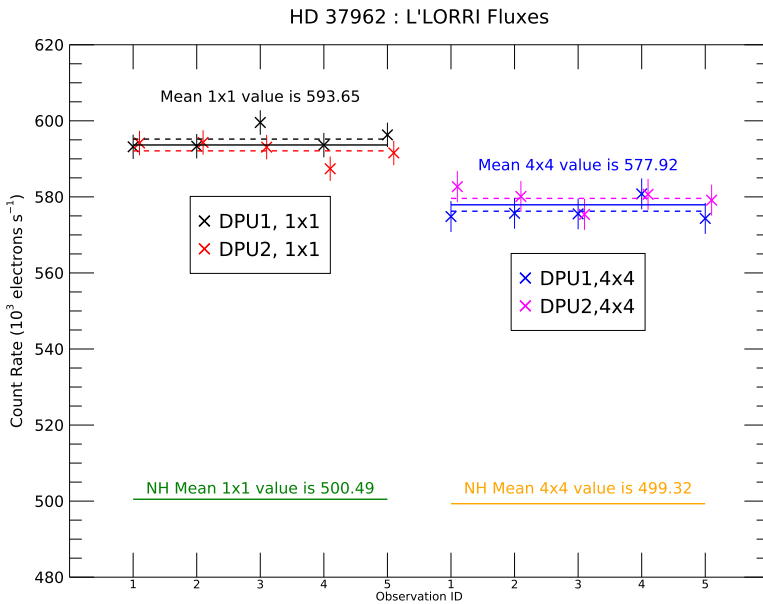


**Fig. 38** L'ORRI observed the absolute calibration star HD 37962 ( $V = 7.810$ ) in February 2022 to measure the total system throughput. The data from both the  $1 \times 1$  and  $4 \times 4$  images, and from both DPUs, are displayed. The two different DPUs give essentially identical results. The signal from the  $1 \times 1$  images is  $\sim 2.7\%$  larger than the signal from the  $4 \times 4$  images, but that is comparable to the uncertainty in converting the measured signal in particular synthetic photometry apertures to the total signal integrated over the PSF. The L'ORRI throughput is  $\sim 19\%$  larger than the throughput from LORRI

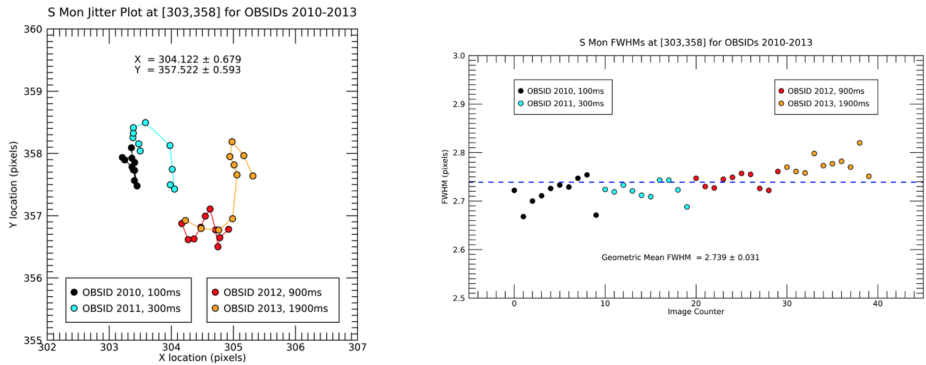


**Fig. 39** The plot on left shows the apparent motion of a star during a series of 40 consecutive images taken in February 2022. The pointing was stable at the level of  $\sim 1$  L'ORRI pixel ( $\sim 1.0''$ ). The plot on the right shows the variation in the PSF FWHM for the 40 images. There is a slight increase in the FWHM with increasing exposure times, but the effect is small

measurements to investigate whether other thermal environments (i.e., colder or warmer OTA temperatures) might improve the PSF.

The observations in May 2022 provided an opportunity to obtain a limited set of data with the OTA at two additional temperatures:  $-75$  C and  $-94$  C. The images at  $-75$  C were more

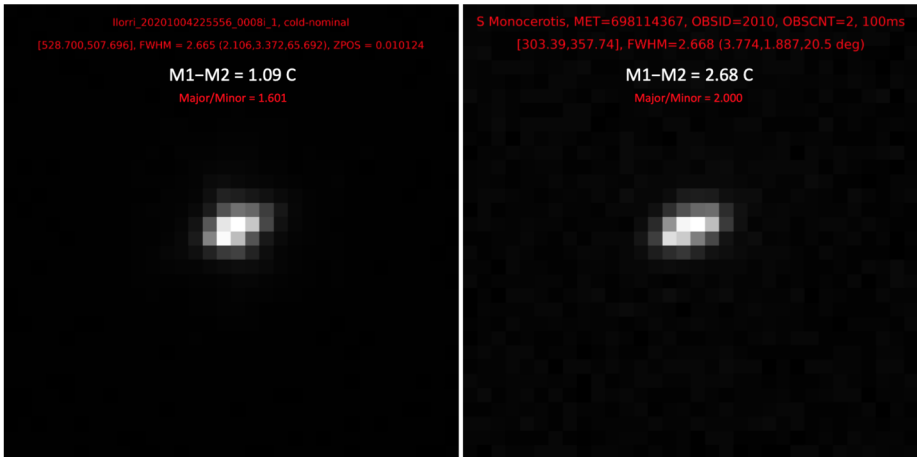


**Fig. 40** The image to the left shows the L’LORRI PSF taken during ground testing with the OTA primary mirror at a temperature of  $-85$  C. The image to the right shows the L’LORRI PSF taken during in-flight observations in February 2022 when the OTA primary temperature was  $-85$  C. Although the two images have similar FWHMs (geometric mean of the best-fit elliptical gaussian is  $\sim 2.7$  pixels in both cases), the in-flight image is considerably more elongated (major/minor ellipse ratio of 2.0 vs 1.6). See the text for further discussion

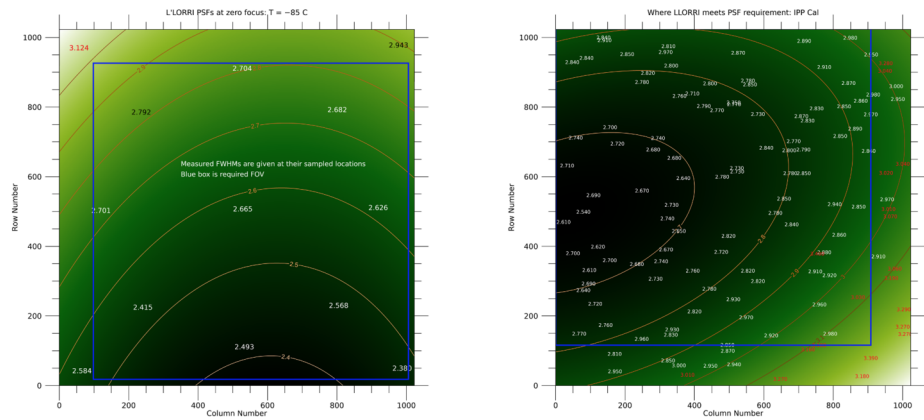


**Fig. 41** The figure to the left plots the FWHM (geometric mean of the best-fit elliptical gaussian) of the L’LORRI PSF over the CCD for images taken during ground testing with the OTA primary mirror at a temperature of  $-85$  C. The figure to the right plots the FWHM of the L’LORRI PSF over the CCD for images taken during in-flight observations in February 2022 when the OTA primary temperature was  $-85$  C. The in-flight FWHMs are generally slightly larger than those obtained during ground testing. The blue boxes in each image show the size of the region where the PSF requirement must be satisfied, which is barely met by the ground case but not quite by the in-flight case. See the text for further discussion

symmetrical (rounder) than the others but were also much broader with FWHMs exceeding 3 pixels everywhere across the FOV because the CCD was far from the optimal focus at that temperature. However, the set of images taken at  $-94$  C had PSFs that looked slightly sharper than those taken at  $-85$  C, which prompted us to select an OTA thermal set point of  $-95$  C for all of the fall 2022 activities, including the observations of NASA’s Double

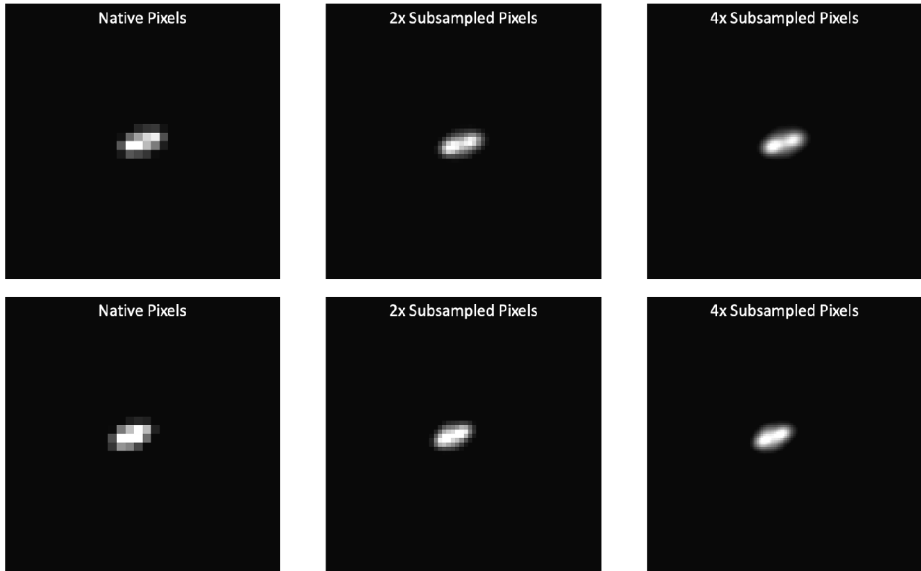


**Fig. 42** Multiple images of a single isolated star have been combined to create Nyquist-sampled versions (Lauer 1999), which have then been displayed in three different formats: with native  $1 \times 1$  pixels, with double-sampled pixels (“2x”), and with quadruple-sampled pixels (“4x”). The top row is derived from data taken in February 2022 when the L’LORRI OTA primary mirror was at  $-85$  C; the bottom row is derived from data taken in October 2022 when the L’LORRI OTA primary mirror was at  $-95$  C. Each image is centered on the pixel with maximum intensity, is displayed on a linear scale from 0 to the maximum value, and covers the same physical area on the CCD. The images at  $-95$  C are more concentrated than those at  $-85$  C suggesting that the resolution is slightly improved at the colder OTA temperature, but all images have a “double star” appearance because the OTA is out-of-focus and has significant astigmatism

Asteroid Redirection Test (DART) impact event and all the observations taken during EGA-1 in mid-October.

For EGA1 (whose observations are discussed in Spencer et al. 2024), we executed an extensive set of observations of the Moon, which provided an opportunity to measure lunar craters with L’LORRI and compare the results to ground truth collected by Moon-orbiting instruments. By taking a set of L’LORRI images of a relatively dense star field shortly after completing the lunar crater program, we created a properly (Nyquist) sampled PSF at  $-95$  C, which could be used to deconvolve the lunar crater images and determine the spatial resolution that might ultimately be achievable during the flybys of the Jovian Trojans. The preliminary analysis of the lunar crater images is reported in an LPSC abstract (Robbins et al. 2023a), and the full analysis has recently been published in a journal (Robbins et al. 2023b).

Figure 42 shows a detailed comparison of the L’LORRI PSF for two OTA temperatures:  $-85$  C and  $-95$  C. In both cases, the PSFs (i.e., the response to a single unresolved target) were constructed from multiple dithered L’LORRI images using a technique described in detail by Lauer (1999) and previously applied successfully to LORRI images of Kerberos (Weaver et al. 2016), one of Pluto’s small satellites. The PSF is clearly more compact for the colder temperature, and we are planning a more extensive set of observations with the OTA at  $-95$  C in the spring of 2023 to determine if that thermal environment should be used for all future L’LORRI observations. On the other hand, even the PSF at  $-95$  C has a “double star” appearance, which will limit the ability of deconvolution methods to squeeze higher resolution out of the L’LORRI images. We were originally expecting deconvolution



to improve the resolution of L'LORRI images by approximately a factor of two, but the lunar crater data suggest that the improvement is likely to be closer to a factor of  $\sqrt{2}$  (Robbins et al. 2023b).

Partly for calibration and partly for scientific purposes, *Lucy* conducted a comprehensive observing program of the Didymos (65803) near-Earth asteroid binary system, starting 12 hr before NASA's DART spacecraft impacted Dimorphos (the satellite of Didymos) and extending to 24 hr after the impact. All observations were performed using L'LORRI  $4 \times 4$  format, and a total of 1549 images were collected documenting the impact event itself and the subsequent evolution of the debris cloud produced during the impact event. A full discussion of the results from the L'LORRI investigation of the DART impact event is provided in a separate publication (Weaver et al. 2023), but preliminary results were reported in Weaver et al. (2022).

## 6 Summary

L'LORRI is the highest resolution imager on the *Lucy* mission. Extensive ground testing of L'LORRI characterized its performance prior to launch, and additional in-flight characterization has been performed during the first year of *Lucy* operations. The total system throughput and CCD performance of L'LORRI have surpassed that provided by *New Horizons* LORRI, the heritage instrument that drove L'LORRI's design. L'LORRI's design goals were not achieved for focus and PSF behavior as a function of temperature; its PSF is considerably broader than LORRI's PSF and has a "double star" appearance that limits its ability to retrieve higher resolution via deconvolution techniques. Nevertheless, the spacecraft-controlled decontamination heater can be used to create a thermal environment that optimizes L'LORRI's optical performance and allows L'LORRI to achieve its scientific objectives. L'LORRI images of its targeted surfaces will reveal their geologies in unprecedented detail and will enable crater counting over several decades of size to constrain surface ages.

Information gleaned from L'LORRI images can be combined with color images and infrared spectral data from the L'Ralph instrument (Reuter et al. 2023) to investigate morphology-composition correlations, including searching for evidence of formerly buried material now on the surface. Morphological data from L'LORRI images can be combined with thermal inertia results derived from L'TES (Christensen et al. 2023) to determine if the surface porosity is associated with particular geological structures. The combination of TTCam (Bell et al. 2024) and L'LORRI imaging of the *Lucy* targets near the time of closest approach will provide important context for the data from both instruments.

L'LORRI will also serve as an excellent optical navigation camera to help guide the *Lucy* spacecraft to its designed aim points for each flyby encounter. During the approach to each *Lucy* target, L'LORRI will perform highly sensitive searches for any potential satellites or rings, as well as dust outflow from the targets that might be suggestive of cometary-like behavior.

The successful launch of *Lucy* on 2021 October 16 marked the beginning of a journey to determine what the Jovian Trojans can reveal about the early history of our solar system, and L'LORRI is expected to play a critical role in that investigation.

### Glossary of Acronyms

ADC	Analog-to-Digital Converter
APL	Applied Physics Laboratory

AR	Anti-Reflection (coating)
ATLO	Assembly, Test, and Launch Operations
au	astronomical unit
CAD	Computer Aided Design
CCD	Charge Coupled Device
CDH	Command and Data Handling
CDS	Correlated Double Sampling
CFS	Common Flight Software
DN	Data Number
DPU	Data Processing Unit
EE	Encircled Energy
EGA	Earth Gravity Assist
FOD	Foreign Object Debris
FOV	Field of View
FPE	Focal Plane Electronics
FPGA	Field Programmable Gate Assembly
FPU	Focal Plane Unit
FWHM	Full Width Half Maximum
I/F	Intensity to (Solar) Flux ratio (reflectance)
IFOV	Instantaneous (single-pixel) Field of View
IPP	Instrument Pointing Platform
JHU	Johns Hopkins University
L3H SSG	L3Harris Sensors and Simulation Group (corporation)
L'LORRI	Lucy Long Range Reconnaissance Imager
LM	Lockheed-Martin (corporation)
LVDS	Low Voltage Differential Signal
LUPI	Laser Unequal Path Interferometer
NASA	National Aeronautics and Space Administration
OCF	Optical Calibration Facility
OpNav	Optical Navigation
OTA	Optical Telescope Assembly
PB	Processor Board
PLRA	Program Level Requirements Appendix
PSF	Point Spread Function
PST	Point Source Transmittance
QE	Quantum Efficiency
SEA	Solar Elongation Angle
SNR	Signal-to-Noise Ratio
STOP	Structural, Thermal, and Optical Performance
TVAC	Thermal Vacuum
V	Visual Magnitude

**Acknowledgements** We thank Aaron Magner, Ray Sterner, Jake Strang, Brian Wolven, Lucas Wray, and Tmitri Zukowski for their critical support of the L'LORRI instrument I&T operations. We thank Dave Cunningham and John Stinchcomb for technical support during I&T, David Jones for leading the EMI-EMC testing, Chi Pham for radiation testing, Maria Spezio for L'LORRI flight software testing, Ryan Tillman for his materials expertise, Shirley Kha for electrical parts support, and Emory Toomey for thermal blanket support and fabrication. We thank the team at L3H (Dave Calabrese, Nangelie Ferrer, Ed Gilbertson, Jim Green, Evan Stryjewski, and Brian Zellers) for their efforts to produce the L'LORRI OTA. We thank the team at Teledyne-e2v (Ross Mackie, Paul Oliver, and Zoe Locke) for providing the L'LORRI CCDs on time. We thank Tod Lauer (NOIRLab) for creating the Nyquist-sampled PSFs. We thank Stefano Mottola for his comments on

a draft of this paper and for his help in creating better L'LORRI flat fields. We gratefully acknowledge the heroic efforts of the *Lucy* personnel at the MOC and SOC who enabled the launch and successful operations of the mission on an extremely tight schedule in the middle of a global pandemic.

**Funding** Financial support for this work was provided by a contract from the Southwest Research Institute to The Johns Hopkins University Applied Physics Laboratory.

## Declarations

**Competing Interests** The authors have no relevant financial or non-financial interests to disclose.

**Open Access** This article is licensed under a Creative Commons Attribution 4.0 International License, which permits use, sharing, adaptation, distribution and reproduction in any medium or format, as long as you give appropriate credit to the original author(s) and the source, provide a link to the Creative Commons licence, and indicate if changes were made. The images or other third party material in this article are included in the article's Creative Commons licence, unless indicated otherwise in a credit line to the material. If material is not included in the article's Creative Commons licence and your intended use is not permitted by statutory regulation or exceeds the permitted use, you will need to obtain permission directly from the copyright holder. To view a copy of this licence, visit <http://creativecommons.org/licenses/by/4.0/>.


## References

- Bell JF III, Zhao Y, Beasley M et al (2024) The terminal tracking camera system on the NASA Lucy Trojan Asteroid Discovery Mission. *Space Sci Rev* 219. <https://doi.org/10.1007/s11214-023-01030-5>
- Cheng AF, Weaver HA, Conard SJ et al (2008) Long-Range Reconnaissance Imager on New Horizons. *Space Sci Rev* 140(1–4):189–215. <https://doi.org/10.1007/s11214-007-9271-6>. arXiv:0709.4278 [astro-ph]
- Cheng AF, Conard SJ, Weaver HA et al (2010) Stray light performance of the long range reconnaissance imager (LORRI) on the New Horizons Mission. In: *Space telescopes and instrumentation 2010: optical, infrared, and millimeter wave*, p 7731 1A. <https://doi.org/10.1117/12.859468>
- Christensen PR, Hamilton VE, Mehall GL et al (2023) The Lucy Thermal Emission Spectrometer (L'TES) Instrument. *Space Sci Rev* 219. <https://doi.org/10.1007/s11214-023-01029-y>
- Evans DW, Riello M, De Angeli F et al (2018) Gaia Data Release 2. Photometric content and validation. *Astron Astrophys* 616:A4. <https://doi.org/10.1051/0004-6361/201832756>. arXiv:1804.09368 [astro-ph.IM]
- Janesick JR (2001) *Scientific charge-coupled devices*. SPIE Press, Bellingham. <https://doi.org/10.1117/3.374903>
- Lauer TR (1999) Combining undersampled dithered images. *Proc Astron Soc Pacific* 111(756):227–237. <https://doi.org/10.1086/316319>. arXiv:astro-ph/9810394 [astro-ph]
- Levison HF, Olkin CB, Noll KS et al (2021) Lucy mission to the Trojan asteroids: science goals. *Planet Sci J* 2(5):171. <https://doi.org/10.3847/PSJ/abf840>
- Levison HF, Marchi S, Noll KS et al (2024) Lucy science and mission overview. *Space Sci Rev* 220
- Nesvorný D, Vokrouhlický D, Morbidelli A (2013) Capture of Trojans by jumping Jupiter. *Astrophys J* 768(1):45. <https://doi.org/10.1088/0004-637X/768/1/45>. arXiv:1303.2900 [astro-ph.EP]
- Noll KS, Brown ME, Buie MW et al (2023) Trojan asteroid satellites, rings, and activity. *Space Sci Rev* 219:59. <https://doi.org/10.1007/s11214-023-01001-w>
- Olkin CB, Vincent M, Adam C et al (2024) Mission design and concept of operations for the Lucy Mission. *Space Sci Rev* 220
- Reuter DC, Simon AA, Lunsford A et al (2023) L'Ralph: a visible/infrared spectral imager for the Lucy Mission to the Trojans. *Space Sci Rev* 219:69. <https://doi.org/10.1007/s11214-023-01009-2>
- Robbins SJ, Bierhaus E, Spencer JR et al (2023a) Testing the ability for deconvolution and Nyquist-sampling to allow detection of small impact craters: lunar proof-of-concept with Lucy's L'LORRI camera. In: *54th Lunar and Planetary Science Conference, LPI Contribution No 2806*, id 2976
- Robbins SJ, Bierhaus EB, Barnouin OS et al (2023b) Imaging Lunar craters with the Lucy Long Range Reconnaissance Imager (L'LORRI): a resolution test for NASA's Lucy Mission. *Planet Sci J*
- Spencer JR, Bell JF III, Christensen PR et al (2024) The first Lucy Earth Flyby (EGA1). *Space Sci Rev* 220
- Weaver HA, Buie MW, Buratti BJ et al (2016) The small satellites of Pluto as observed by New Horizons. *Science* 351(6279):aae0030. <https://doi.org/10.1126/science.aae0030>. arXiv:1604.05366 [astro-ph.EP]

- Weaver HA, Cheng AF, Morgan F et al (2020) In-flight performance and calibration of the LOng Range Reconnaissance Imager (LORRI) for the New Horizons Mission. *Proc Astron Soc Pacific* 132(1009):035003. <https://doi.org/10.1088/1538-3873/ab67ec>. arXiv:2001.03524 [astro-ph.IM]
- Weaver HA, Spencer JR, Marchi S et al (2022) Investigating the DART impact event with the Lucy LOng Range Reconnaissance Imager. In: AGU fall meeting abstracts, pp P54C–01
- Weaver HA, Spencer JR, Marchi S et al (2023) Lucy observations of the DART impact event. *Planet Sci J*

**Publisher's Note** Springer Nature remains neutral with regard to jurisdictional claims in published maps and institutional affiliations.

## Authors and Affiliations

H.A. Weaver<sup>1</sup>  · J.P. Wilson<sup>1</sup> · S.J. Conard<sup>1</sup> · J.D. Adams<sup>1</sup> · S. Begley<sup>1</sup> · J. Burgum<sup>1</sup> · E.H. Darlington<sup>1</sup> · N. Dello Russo<sup>1</sup> · R. Hacala<sup>1</sup> · S. London<sup>1</sup> · M.F. Morgan<sup>1</sup> · G. Murphy<sup>1</sup> · T. Nelson<sup>1</sup> · A. Shah<sup>1</sup> · J.R. Spencer<sup>2</sup> · H. Taylor<sup>1</sup> · T. Boehmer<sup>1</sup> · L. Burke<sup>1</sup> · C. Drabenstadt<sup>1</sup> · C. Henry<sup>1</sup> · S. Ling<sup>1</sup> · C. Porter<sup>1</sup> · J. Yin<sup>1</sup>

- ✉ H.A. Weaver  
[hal.weaver@jhuapl.edu](mailto:hal.weaver@jhuapl.edu)
- J.P. Wilson  
[john.wilson@jhuapl.edu](mailto:john.wilson@jhuapl.edu)
- S.J. Conard  
[steven.conard@jhuapl.edu](mailto:steven.conard@jhuapl.edu)
- J.D. Adams  
[dewey.adams@jhuapl.edu](mailto:dewey.adams@jhuapl.edu)
- S. Begley  
[shawn.begley@jhuapl.edu](mailto:shawn.begley@jhuapl.edu)
- J. Burgum  
[james.burgum@jhuapl.edu](mailto:james.burgum@jhuapl.edu)
- E.H. Darlington  
[hugo.darlington@jhuapl.edu](mailto:hugo.darlington@jhuapl.edu)
- N. Dello Russo  
[neil.dello.russo@jhuapl.edu](mailto:neil.dello.russo@jhuapl.edu)
- R. Hacala  
[ryan.hacala@jhuapl.edu](mailto:ryan.hacala@jhuapl.edu)
- S. London  
[shaughn.london@jhuapl.edu](mailto:shaughn.london@jhuapl.edu)
- M.F. Morgan  
[frank.morgan@jhuapl.edu](mailto:frank.morgan@jhuapl.edu)
- G. Murphy  
[graham.murphy@jhuapl.edu](mailto:graham.murphy@jhuapl.edu)
- T. Nelson  
[tyler.nelson@jhuapl.edu](mailto:tyler.nelson@jhuapl.edu)
- A. Shah  
[amit.shah@jhuapl.edu](mailto:amit.shah@jhuapl.edu)
- J.R. Spencer  
[spencer@boulder.swri.edu](mailto:spencer@boulder.swri.edu)
- H. Taylor  
[howard.taylor@jhuapl.edu](mailto:howard.taylor@jhuapl.edu)

T. Boehmer  
[tyler.boehmer@jhuapl.edu](mailto:tyler.boehmer@jhuapl.edu)

L. Burke  
[linda.burke@jhuapl.edu](mailto:linda.burke@jhuapl.edu)

C. Drabenstadt  
[christian.drabenstadt@jhuapl.edu](mailto:christian.drabenstadt@jhuapl.edu)

C. Henry  
[charles.henry@jhuapl.edu](mailto:charles.henry@jhuapl.edu)

S. Ling  
[sharon.ling@jhuapl.edu](mailto:sharon.ling@jhuapl.edu)

C. Porter  
[christa.porter@jhuapl.edu](mailto:christa.porter@jhuapl.edu)

J. Yin  
[jie.yin@jhuapl.edu](mailto:jie.yin@jhuapl.edu)

<sup>1</sup> Space Exploration Sector, Johns Hopkins University Applied Physics Laboratory, 11100 Johns Hopkins Road, Laurel, 20723-6099, MD, USA

<sup>2</sup> Department of Space Studies, Southwest Research Institute, 1050 Walnut Street, Suite 300, Boulder, 80302, CO, USA